

AD_____

CONTRACT NUMBER DAMD17-94-C-4102

TITLE: Develop a Small Mobile Robot Along With Piezoelectric Ultrasonic Motors Which Can Be Made Compact For Use On a Small Robot

PRINCIPAL INVESTIGATION: Massachusetts Institute

CONTRACTING ORGANIZATION: Massachusetts Institute of Technology
Cambridge, Massachusetts 02139-4307

REPORT DATE: July 1996

DTIC QUALITY INSPECTED 4

TYPE OF REPORT: Final

PREPARED FOR: Commander
U.S. Army Medical Research and Materiel Command
Fort Detrick, Frederick, Maryland 21702-5012

DISTRIBUTION STATEMENT: Approved for public release;
distribution unlimited

The views, opinions and/or findings contained in this report are those of the author(s) and should not be construed as an official Department of the Army position, policy or decision unless so designated by other documentation.

19960820 081

DISCLAIMER NOTICE



THIS DOCUMENT IS BEST QUALITY AVAILABLE. THE COPY FURNISHED TO DTIC CONTAINED A SIGNIFICANT NUMBER OF PAGES WHICH DO NOT REPRODUCE LEGIBLY.

REPORT DOCUMENTATION PAGE

Form Approved
OMB No. 0704-0188

Public reporting burden for this collection of information is estimated to average 1 hour per response, including the time for reviewing instructions, searching existing data sources, gathering and maintaining the data needed, and completing and reviewing the collection of information. Send comments regarding this burden estimate or any other aspect of this collection of information, including suggestions for reducing this burden, to Washington Headquarters Services, Directorate for Information Operations and Reports, 1215 Jefferson Davis Highway, Suite 1204, Arlington, VA 22202-4302, and to the Office of Management and Budget, Paperwork Reduction Project (0704-0188), Washington, DC 20503.

1. AGENCY USE ONLY (Leave blank)	2. REPORT DATE July 1996	3. REPORT TYPE AND DATES COVERED Final (16 Sep 94 - 31 May 96)	
4. TITLE AND SUBTITLE Develop a Small Mobile Robot Along With Piezoelectric Ultrasonic Motors Which Can Be Made Compact For Use On a Small Robot		5. FUNDING NUMBERS DAMD17-94-C-4102	
6. AUTHOR(S) Massachusetts Institute			
7. PERFORMING ORGANIZATION NAME(S) AND ADDRESS(ES) Massachusetts Institute of Technology Cambridge, Massachusetts 02139-4307		8. PERFORMING ORGANIZATION REPORT NUMBER	
9. SPONSORING/MONITORING AGENCY NAME(S) AND ADDRESS(ES) Commander U.S. Army Medical Research and Materiel Command Fort Detrick, Frederick, MD 21702-5012		10. SPONSORING/MONITORING AGENCY REPORT NUMBER	
11. SUPPLEMENTARY NOTES			
12a. DISTRIBUTION / AVAILABILITY STATEMENT Approved for public release; distribution unlimited		12b. DISTRIBUTION CODE	
13. ABSTRACT (Maximum 200) This report describes research undertaken to develop mechanisms for telepresence surgery and the basic technologies that would enable a surgeon to direct a self-propelled endoscope through a patient's large intestine from a remote location. Three omni-directional belt-driven prototypes were built and driven through an intestine-like environment. In addition, enabling technologies of thick-film PZT and 8mm ultrasonic motors were developed. The latter demonstrated stall torque densities 50 times those of comparably-sized electromagnetic DC motors.			
14. SUBJECT TERMS autonomous endoscope; ultrasonic motors; thick-film PZT			15. NUMBER OF PAGES 58
			16. PRICE CODE
17. SECURITY CLASSIFICATION OF REPORT Unclassified	18. SECURITY CLASSIFICATION OF THIS PAGE Unclassified	19. SECURITY CLASSIFICATION OF ABSTRACT Unclassified	20. LIMITATION OF ABSTRACT Unlimited

Table of Contents

Introduction	2
Body	3
Intestine Crawler Prototypes	3
Printed Circuit Board Level Integrated Machines	4
Miniature Ultrasonic Motors	5
Design of Experiments	7
Comparisons to Other Actuator Technologies	12
Thick Film PZT: Penn State Materials Research Laboratory	14
Overview	14
Experimental Methods	15
Results	16
Summary	22
Conclusions	23
Autonomous Endoscopes and Ultrasonic Motors	23
Thick Film PZT	23
References	24
Appendix A: Autonomous Endoscope Propulsion	25

Introduction

This final report describes results of research undertaken in a collaboration between the MIT Artificial Intelligence Laboratory and the Pennsylvania State University's Materials Research Laboratory to develop mechanisms for telepresence surgery and the basic technologies that would enable a surgeon to direct a self-propelled endoscope through a patient's large intestine from a remote location.

Surgeons today use manually-operated endoscopes to view organs deep inside the human body. These scopes are awkward to use, have limited visualization capability except directly forward of the endoscope tip and are often unable to be coerced around bends or into cavities not firmly tacked down, such as the small intestine. There is a need for a self-propelled endoscope that could maneuver its way through difficult terrain, transmitting images and performing tasks as directed by the surgeon, both to create a more patient-friendly procedure and to enable the surgeon to perform minimally invasive techniques in locations not previously possible.

At the MIT Artificial Intelligence Laboratory, prior to the start of this project, we had had 10 years of experience in building self-contained autonomous mobile robots which exhibited task-achieving behaviors using subsumption style intelligence architectures. With these computationally lean control systems, we had been able to create dozens of the world's smallest robots. From this technology base, we proposed to develop mechanisms for autonomous endoscope propulsion along with actuators that would enable miniaturization.

This report describes the mechanisms that were investigated and details the most successful approaches. A more detailed account is included in Appendix A, which illuminates the process of the investigation and a number of autonomous endoscope prototypes which were not as successful. This report then goes on to detail extensive research into ultrasonic minimotors and new materials that were developed under this program for the purpose of enabling the large prototype autonomous endoscopes to be scaled to a size amenable to use in a patient.

We have developed a new type of actuator, an 8 mm diameter by 3 mm tall piezoelectric ultrasonic motor, which exhibits a factor of 50 improvement in stall torque density over the smallest commercially available component motors today. These motors give us the capability now of building miniature robotic vehicles smaller than ever previously possible. In addition, through the Penn State Materials Research Laboratory, we have also performed basic research in developing new piezoelectric materials for incorporation onto silicon substrates, enabling the future possibility of integrated drive electronics with the actual motor itself.

Body

One of the main difficulties in creating a self-propelled camera the size of a thumb which can crawl through intestines is the dearth of small actuators with the proper speed-torque requirements for the task. Using conventional electromagnetic motors, even the smallest available, typically entails that the locomoting vehicle be a one or two degree-of-freedom machine with extensive gearing, discrete linkages and novel transmission systems. Furthermore, due to the slippery gooey environment, some type of skin or sheathing is required to protect the mechanisms. Even more importantly, due to the risks of infection, the sheath, or even the entire mechanism, may need to be disposable.

Intestine Crawler Prototypes

Figure 1 illustrates intestine-crawling devices developed under this DARPA-sponsored autonomous endoscope project. While 20 or 30 designs were investigated and prototyped, these three demonstrated the most success. Clearly, significant advances must be made in miniaturization to create a vehicle which will painlessly traverse the large intestine. Nevertheless, the devices give us feedback on locomotion options.

The device at left in Figure 1 is a single degree-of-freedom machine in which a large central worm drives a number of paddle wheels mounted in a concentric cylinder. While the paddle wheels grab the sides of the intestines (chicken skins were used in actual tests) at many points around the periphery, they also tend to pinch the skin and pull it into the paddles.

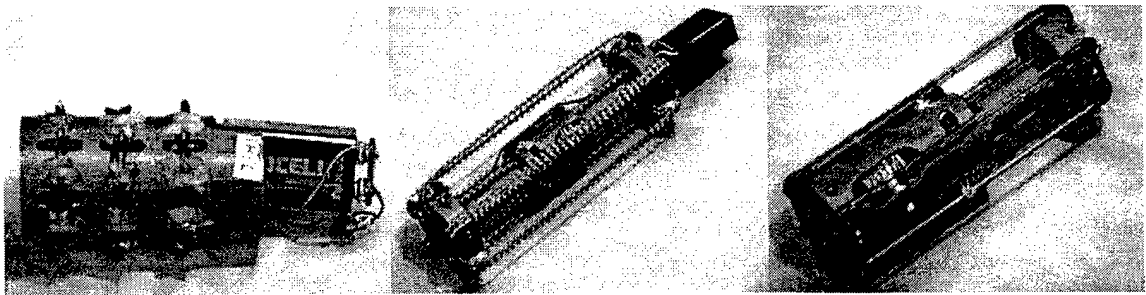


Figure 1. Intestine crawler prototypes designed for evaluation of locomotion mechanisms. All are single degree-of-freedom devices. a) At left, a single DC motor in an internal central worm drives a number of paddle wheels mounted in a cylindrical shell. b) Two 10 mm diameter gearhead motors drive six belts each around pulleys to create an omni-directional tractor (center). c) At right, a single 10 mm diameter gearhead motor drives all six belts in a machine half the size of b).

The device in the center uses two 10 mm diameter motors with a stall torque of 0.15 oz.-in. (1.1 mNm) with a geardown of 30,720 on each motor. Each motor drives three belted track mechanisms which propel the vehicle through the chicken-skin tube at a lumbering 2 mm/sec. This machine is rather large at 15 cm long and 5.5 cm in diameter, although

clearly the most proficient. Figure 2 shows this prototype crawling through chicken skins sutured into a tube with staples and resting on a non-rigidly supported jello substrate.

The vehicle at right in Figure 1 is a half-size version of the previous device. It utilizes a single 10 mm diameter motor with a gear-down of 15,360 driving all six belts. This machine fared poorly, one of the reasons being that the aspect ratio of major and minor diameters in these omni-directional tracked vehicles was found to be critical. That is, the diameter of the vehicle measured to the outer edge of the pulleys, as compared to the diameter of the structural cylinder, corresponds to the amount of traction created versus frictional drag from the central hub as the intestines collapse in on the crawler. More details of the design and earlier prototypes can be found in [Shectman 95], excerpts of which are included in Appendix A.

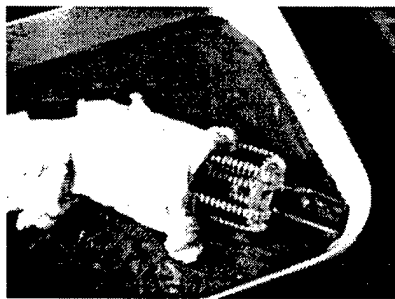


Figure 2. The intestine crawler of b) in the previous figure is shown here crawling through a simulated intestinal environment. Chicken skins are used for testing.

Printed Circuit Board Level Integrated Machines

While the locomotion mechanism is critical in developing a self-propelled machine that will traverse the large intestine, control issues, integration of electronics, mechanics and software, and packaging also need to be worked out. In addition to these aforementioned development of locomotion mechanisms, we have undertaken extensive efforts in this program to develop integrated machines at the printed circuit board level. Figure 3 shows one of 12 small robots that were developed, using commercially available DC motors manufactured by Namiki Corporation, and which have a chassis and motor-mount construction technique which consists entirely of printed circuit boards which also hold all the sensors, drive electronics, intelligence and batteries. These small robots, which fit in the palm of one's hand, are programmed in on-board EEPROM with subsumption architecture control programs which endow them with behaviors for avoiding obstacles, picking up food, cooperating on tasks and finding home. Similar styles of subsumption control programs would be used for the basic behaviors on the surgeon's remotely operated endoscope, whereby the surgeon would command tasks such as moving forward, grabbing a piece of tissue, etc., and the on-board software would direct subsequent motor actions. Further details on the robots illustrated in Figure 3 can be found in [McLurkin 95].

Miniature Ultrasonic Motors

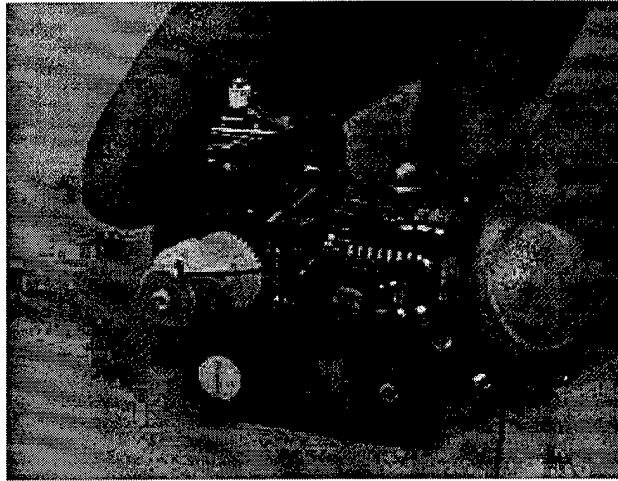


Figure 3. Weighing in at 1.3 ounces, this robot is equipped with 2 bump sensors, 4 light sensors, 4 infrared communications receivers, 5 food sensors, a tilt sensor, a battery, a DC-DC converter, a serial port, 3 motors and a gripper.

In parallel with these investigations into locomotion mechanisms, we performed an extensive study and development effort in modeling and fabrication of a family of 8 mm diameter ultrasonic motors in a designed experiment. An ultrasonic motor consists of a stator and a rotor. The stator is made by bonding a thin layer of piezoelectric material, electroded in an appropriate pattern, to a non-piezoelectric ring. The piezoelectric layer is driven so as to induce a traveling wave of bending in the ring, which in turn causes any point on the surface of the ring to move in a retrograde elliptical motion. This vibrational motion is converted to a macroscopic motion of the rotor when the rotor is physically pressed against the stator, where frictional forces pull the rotor along. Figure 4 shows results of analysis and simulations that were undertaken and illustrates the 3-wavelength bending mode for which the 8 mm stators in this study were designed.

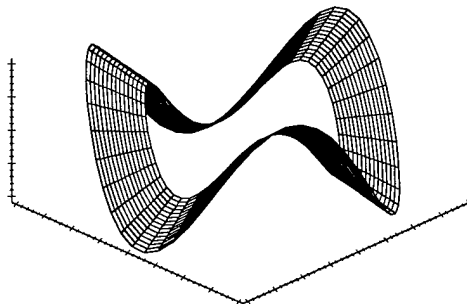


Figure 4. A Rayleigh-Ritz model of the cylindrical laminated thin plate stator predicts deflections of the stator and consequent speed, torque, power and efficiency of the ultrasonic motor.

Photographs of one of the motors fabricated are shown in Figure 4. A rotor sits atop the stator at left and the stator alone is shown at right. Traveling flexure waves are induced to propagate around the ring by bulk ceramic lead zirconated titanate (PZT) piezoelectric material bonded to the bottom of the stator and electroded appropriately. Second generation 8 mm bulk-PZT ultrasonic motors with improved electrode designs were able to achieve an order-of-magnitude improvement in out-of-plane stator displacement as compared to first-generation motors. Out-of-plane displacements in the second generation motors, measured interferometrically, was on the order of 6 μm .

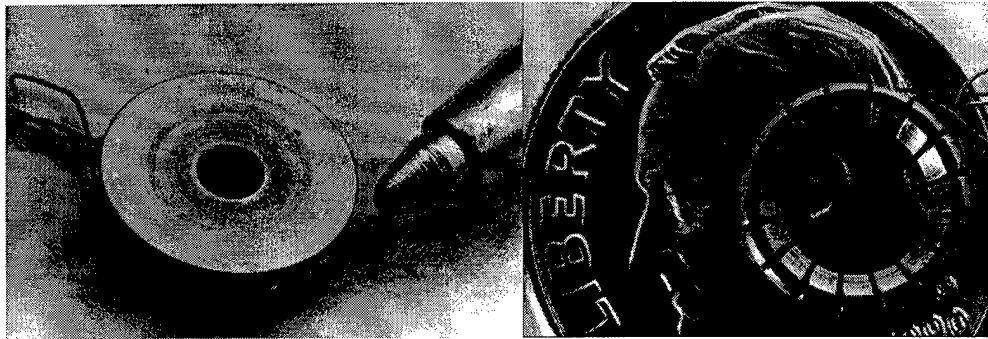


Figure 5. 8 mm ultrasonic motors. Surface finish conditions are important as asperity height must be much less than the out-of-plane displacement of the stator.

Shown below is a measured speed-torque characteristic for one 8 mm diameter by 3 mm tall steel stator ring bonded onto a bulk PZT piece patterned to induce a three-wavelength traveling flexure wave when driven with two-phase 60 V_{peak} excitation. A sapphire disk was used for the rotor. Peak power was measured to be 16 mW.

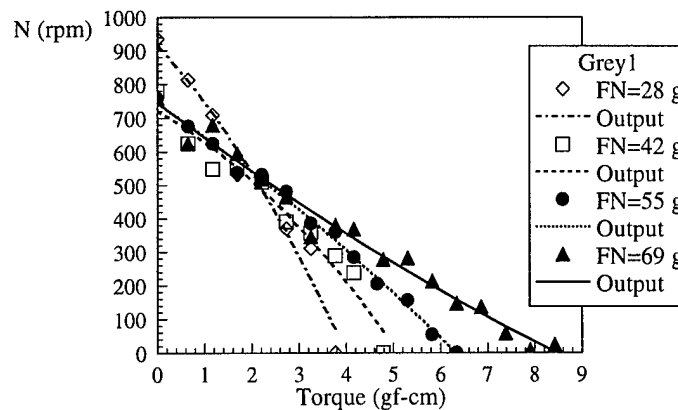


Figure 6. Speed-torque curve of our 8 mm ultrasonic motor. A suite of motors was created in a designed experiment. Stall torques as large as 1 mNm were seen.

Design of Experiments

The motor and resulting data shown above were just one trial in a more extensive suite of experiments performed with Design of Experiments methods [Fieguth et al. 94]. Other motors in the designed experiment showed peak powers as high as 28 mW and stall torques as large as 10 gf-cm, or 1 mNm. Extensive detail on the ultrasonic minimotor effort can be found in [Flynn 95]. Manufacturing techniques, perfected in the third and fourth generation motors, are described in [Franck 95].

The designed experiment was set up as a 32-trial experiment where each trial represented a rotor-stator combination and maximum no-load speed and maximum stall torque was measured. These variables were measured on a dynamometer custom-built for this research effort and manufactured by Ceteor in Besancon, France. The normal force between the stator and rotor was adjusted in each trial to find the maximum stall torque and no-load speeds. Each motor was run at its resonant frequency with a peak voltage of 60 V and the two phases of the drive signal were set 90 degrees apart.

Seven factors were varied in the overall experiment, allowing for 2^7 possible trials. Design of Experiments techniques allow for collecting appropriate data which can be analyzed by statistical methods for formulating objective conclusions with fewer than the complete number of all possible trials. In this case, we use a one-quarter factorial design, or 2^5 trials. Of the seven factors varied, 4 pertained to the stator and 3 to the rotor. The 4 stator parameters were the tooth height, the base height, the number of teeth and the stator material. For the rotor, we varied the rotor material, rotor liner and lubrication. Figure 7 displays the notation (+ or -) used to represent each binary possibility.

Figure 8 illustrates the appropriate mapping of the 2^5 combinations. The first three factors, tooth height, base height and the number of teeth (denoted v_1 , v_2 and v_3 respectively) are assigned all possible (2^3) combinations of levels. The fourth factor, the stator material, is assigned to the combination that is equivalent to the interaction between v_2 and v_3 , which is assumed insignificant. Note that column v_{23} is the product of

Parameters			
		-	+
1	Tooth Height	30 mils (0.76 mm)	50 mils (1.3 mm)
2	Base Height	10 mils (0.25 mm)	15 mils (0.38 mm)
3	#Teeth	24	36
4	Stator Material	6061 Aluminum	304 Stainless Steel
5	Rotor Liner	None	Kapton
6	Rotor Material	Hardened O1 Tool Steel	Sapphire
7	Lubricant	None	WD-40 Oil

Figure 7. The stator and rotor parameters in the designed experiment are one of two possibilities each.

columns v_2 and v_3 . In this way, four parameters can be studied with 8 runs. The average column is also included to account for common mode results in each trial. Row 1 signifies a motor trial where the stator has a tooth height of 50 mils, a base height of 15 mils, 36 teeth and

8 mm Bulk PZT Ultrasonic Motor Experiment Design									
		Avg	v_1	v_2	v_3	v_{23}	v_4	v_5	v_6
			Tooth	Base	#Teeth	Smat	Liner	Rmat	Oil
1	Violet	+	+	+	+	+	+	+	+
2		+	+	+	+	+	+	+	-
3		+	+	+	+	+	+	-	+
4		+	+	+	+	+	+	-	-
5	Fucia	+	+	+	-	-	+	+	+
6		+	+	+	-	-	+	+	-
7		+	+	+	-	-	+	-	+
8		+	+	+	-	-	+	-	-
9	Tan	+	+	-	+	-	-	+	+
10		+	+	-	+	-	-	+	-
11		+	+	-	+	-	-	-	+
12		+	+	-	+	-	-	-	-
13	Blue	+	+	-	-	+	-	+	+
14		+	+	-	-	+	-	+	-
15		+	+	-	-	+	-	-	+
16		+	+	-	-	+	-	-	-
17	Green	+	-	+	+	+	-	+	+
18		+	-	+	+	+	-	+	-
19		+	-	+	+	+	-	-	+
20		+	-	+	+	+	-	-	-
21	Yellow	+	-	+	-	-	-	+	+
22		+	-	+	-	-	-	+	-
23		+	-	+	-	-	-	-	+
24		+	-	+	-	-	-	-	-
25	Orange	+	-	-	+	-	+	+	+
26		+	-	-	+	-	+	+	-
27		+	-	-	+	-	+	-	+
28		+	-	-	+	-	+	-	-
29	Grey	+	-	-	-	+	+	+	+
30		+	-	-	-	+	+	+	-
31		+	-	-	-	+	+	-	+
32		+	-	-	-	+	+	-	-

Figure 8. This one-quarter fraction factorial design selects 32 trials out of a possible 2^7 . The 4-row blocks given names as the colors violet, fucia, tan, blue, green, yellow, orange and grey, signify the 8 different stators that we have manufactured.

is made out of steel. The rotor is sapphire with a kapton liner and has a WD-40 oil lubricant. Row 2 signifies the same stator and same rotor, but no lubrication and so on. Figure 9 lists the measured results for each trial. It was found that the motors did not work at all when WD-40 lubricant was applied. Consequently, every other row in the table has a zero result. This means that the matrix can be recast as a 16-trial experiment where the oil parameter is removed as shown in Figure 10, where the frequency and normal forces are also noted.

Design of Experiments Results: Stall Torques and No-load Speeds						
	Stator	Liner	Rmat	Oil	Max Stall Torque (gf-cm)	Max No-load Speed (rpm)
1	Violet Exp 1	+	+	+	0	0
2	Violet Exp 2	+	+	-	4.7	1660
3	Violet Exp 3	+	-	+	0	0
4	Violet Exp 4	+	-	-	4.8	1600
5	Fucia Exp 1	+	+	+	0	0
6	Fucia Exp 2	+	+	-	5.5	1750
7	Fucia Exp 3	+	-	+	0	0
8	Fucia Exp 4	+	-	-	4.5	1610
9	Tan Exp 1	-	+	+	0	0
10	Tan Exp 2	-	+	-	2.7	746
11	Tan Exp 3	-	-	+	0	0
12	Tan Exp 4	-	-	-	3.4	893
13	Blue Exp 1	-	+	+	0	0
14	Blue Exp 2	-	+	-	4.7	787
15	Blue Exp 3	-	-	+	0	0
16	Blue Exp 4	-	-	-	4.8	813
17	Green Exp 1	-	+	+	0	0
18	Green Exp 2	-	+	-	10.0	870
19	Green Exp 3	-	-	+	0	0
20	Green Exp 4	-	-	-	8.4	781
21	Yellow Exp 1	-	+	+	0	0
22	Yellow Exp 2	-	+	-	5.3	800
23	Yellow Exp 3	-	-	+	0	0
24	Yellow Exp 4	-	-	-	5.6	840
25	Orange Exp 1	+	+	+	0	0
26	Orange Exp 2	+	+	-	4.8	1060
27	Orange Exp 3	+	-	+	0	0
28	Orange Exp 4	+	-	-	4.6	1100
29	Grey Exp 1	+	+	+	0	0
30	Grey Exp 2	+	+	-	4.3	885
31	Grey Exp 3	+	-	+	0	0
32	Grey Exp 4	+	-	-	5.3	901

Figure 9. Resulting stall torques and no-load speeds for the designed experiment.

Design of Experiments Results: Stall Torques and No-load Speeds								
	Stator	Liner	Rmat	Frequency (kHz)	Max Stall Torque (gf-cm)	@FN (gf)	Max No-load Speed (rpm)	@FN (gf)
1	Violet Exp 2	+	+	44.5	4.7	62	1660	6.9
2	Violet Exp 4	+	-	44.5	4.8	66	1600	11
3	Fucia Exp 2	+	+	55.5	5.5	81	1750	11
4	Fucia Exp 4	+	-	55.5	4.5	97	1610	4.8
5	Tan Exp 2	-	+	38.0	2.7	38	746	4.1
6	Tan Exp 4	-	-	38.0	3.4	40	893	21
7	Blue Exp 2	-	+	35.5	4.7	76	787	35
8	Blue Exp 4	-	-	35.5	4.6	83	813	14
9	Green Exp 2	-	+	57.7	10.0	110	870	6.9
10	Green Exp 4	-	-	57.7	8.4	110	781	30
11	Yellow Exp 2	-	+	63.0	5.3	66	800	6.9
12	Yellow Exp 4	-	-	63.0	5.6	59	840	2.8
13	Orange Exp 2	+	+	47.4	4.8	97	1060	17
14	Orange Exp 4	+	-	47.4	4.6	97	1100	14
15	Grey Exp 2	+	+	42.2	4.3	94	885	17
16	Grey Exp 4	+	-	42.2	5.3	110	901	14

Figure 10. Resulting stall torques and no-load speeds for the designed experiment with the oil parameter removed. Stator Green, in combination with an unlined sapphire rotor and no lubricant, produced the largest stall torque: 10 gf-cm. Stator Fucia, with a kapton-coated sapphire rotor and no lubricant, produced the highest no-load speed: 1750 rpm.

Figure 10 shows that stator Green (0.76 mm tooth height, 0.38 mm base height, 36 teeth, made out of stainless steel), in combination with an unlined sapphire rotor and no lubricant, produced the largest stall torque: 10.0 gf-cm. Stator Fucia (1.3 mm tooth height, 0.38 mm base height, 24 teeth, made out of aluminum), with a kapton-coated sapphire rotor and no lubricant, produced the highest no-load speed: 1750 rpm.

The analysis was performed using a software tool [Fieguth et al. 94] developed in the MIT Leaders for Manufacturing Program which not only determines the weights for a predictor polynomial, but also performs a search through the parameter space for the optimal combination of parameters (the predictor variable string) to minimize the quality factor measured. For details on the predictor polynomial calculated, see [Flynn 95]. The predictor variable string calculated for maximum stall torque was “-+++-+”, which refers to stator Green, with an unlined sapphire rotor as the optimal configuration for maximizing stall torque. This combination happens to be one of the trials performed, but in general the predictor string could have been an untried combination.

The predictor string for maximum no-load speed was “+++-+-”, which was a different combination than any of the trial motors built. This suggests that the next experiment would be to fabricate such a stator: tall teeth, large base height, large number of teeth,

Design of Experiments Results: Stall Torque Densities						
	Stator	Max Stall Torque (gf-cm)	Mass (g) St+Rot= Tot	Volume (mm ³)	Max Stall Torque Density (Nm/kg)	Max Stall Torque Density (gf-cm/mm ³)
1	Violet Exp 2	4.7	.28+.13=.41	120	1.2	0.039
2	Violet Exp 4	4.8	.28+.37=.65	120	0.74	0.040
3	Fucia Exp 2	5.5	.13+.13=.26	120	2.1	0.046
4	Fucia Exp 4	4.5	.13+.37=.50	120	0.90	0.038
5	Tan Exp 2	2.7	.12+.12=.24	87	1.1	0.031
6	Tan Exp 4	3.4	.12+.36=.48	87	0.71	0.039
7	Blue Exp 2	4.7	.27+.12=.39	87	1.2	0.054
8	Blue Exp 4	4.6	.27+.36=.60	87	0.77	0.053
9	Green Exp 2	10.0	.22+.12=.34	68	2.9	0.15
10	Green Exp 4	8.4	.22+.36=.58	68	1.5	0.12
11	Yellow Exp 2	5.3	.11+.12=.23	68	2.3	0.078
12	Yellow Exp 4	5.6	.11+.36=.47	68	1.2	0.082
13	Orange Exp 2	4.8	.10+.13=.23	61	2.1	0.079
14	Orange Exp 4	4.6	.10+.37=.47	61	1.0	0.075
15	Grey Exp 2	4.3	.20+.13=.33	61	1.3	0.070
16	Grey Exp 4	5.3	.20+.37=.57	61	0.93	0.087

Figure 11. Stall torque densities resulting from the 16-trial experiment of 8 mm bulk PZT ultrasonic motors. Stator Green1 (short teeth, thick base, 36 teeth, stainless steel) with a plain sapphire rotor produced 2.9 Nm/kg stall torque density.

made out of aluminum, with a kapton-coated sapphire rotor, and check.

By comparing the measured maximum stall torques and output powers by the weight or volume of the stator-rotor assembly, we can examine figures of merit for our motors. [Hollerback et al. 91] argue that the most useful figure of merit for comparing disparate motor technologies is stall torque density (Nm/kg) as power density figures really depend on the associated power electronics.

Figure 11 lists the stall torque densities resulting from our 16-trial experiment. The maximum stall torque density of 2.9 Nm/kg is produced by stator Green1 with a sapphire rotor. Note that the motors here do not have bearings and mounts, but are held together in a dynamometer. We have put off working on bearing and mounts until the motors were better understood and useful torques could be shown. This has now been achieved and in the near future we will attach a simple bearing to one of these motors.

Power Density							
Stator	Liner	Rmat	Mass (g) St+Rot= Tot	Volume (mm ³)	Peak Power (mW)	Peak Power Density (W/kg)	Peak Power Density (mW/mm ³)
Fucia	-	+	.13+.12=.25	120	27	108	0.23
Yellow Exp 2	-	+	.11+.12=.23	88	12	52	0.18
Grey	-	+	.20+.12=.32	61	16	50	0.26

Figure 12. Output power densities for the second generation motors. Power densities as high as 108 W/kg have been achieved with stator Fucia1 (tall teeth, thick base, 24 teeth, aluminum) with a plain sapphire rotor.

Figure 12 lists the corresponding output power densities for the 8 mm motors. Stator Fucia1 with a sapphire rotor produced the highest power density of 108 W/kg.

Comparisons to Other Actuator Technologies

Actuator	Power Dens (W/kg)	Stall Torque Dens (Nm/kg)
McGill/MIT EM Motor	15	200
Sarcos Dextrous Arm electro-hydraulic rotary actuator	120	600
Utah/MIT Dextrous Hand electropneumatic servovalve	20	200
NiTi SMA [Hirose 89]	1	6
PVA-PAA polymeric actuator [Caldwell 90]	17	6
Burleigh Instruments inch worm piezoelectric motor	3	0.1
Magnetoelastic (magnetostrictive) wave motor [Kiesewetter 88]	500	5
Human biceps muscle	20	50
MIT 8 mm Fucia/Green	108	2.9

Figure 13. Power density and stall torque density can be used as figures-of-merit to compare actuator technologies.

It is interesting to compare piezoelectric ultrasonic motors and see how other actuator technologies measure up. Figure 13, amended from [Hollerbach et al. 91], shows how a wide variety of technologies, such as hydraulic systems, pneumatic actuators, shape memory alloys, piezoelectric inchworms, magnetostrictive materials and human muscle compare in terms of both stall torque density and output power density. We have inserted our recent results into their table where the number for power density refers to the stator Fucia1 running on a plain sapphire rotor and the number for stall torque density refers to the stator Green1 also running with a plain sapphire rotor.

Note that the piezoelectric ultrasonic motors vastly outperform the piezoelectric inchworm drives. This is due to the fact that resonance is used to advantage in the ultrasonic motors, whereas the inchworm drives are quasistatic.

While the stall torque densities for the first three actuators in the table are significantly higher than those for our ultrasonic motors, it is useful to note that these are all fairly large actuators. The McGill/MIT electromagnetic motor is also water-cooled. If we compare our 8 mm ultrasonic motors to small DC motors that would typically be the direct competition, our ultrasonic motors compare exceedingly well.

Figure 14 gives figures of merit comparing ultrasonic motors reported in the literature with small electromagnetic DC motors typically used in mobile robot applications. The first six motors listed in Figure 14 are electromagnetic motors, the next four are larger Japanese ultrasonic motors, on the order of 40 to 60 mm in diameter.

The smallest commercially available electromagnetic DC motor is the Namiki 7CL-1701. This is the motor that is used in the robot shown in Figure 3 for each of the drive wheels and the gripper. It is 7 mm in diameter and 18 mm long, roughly 5 times the volume of our 8 mm ultrasonic motors, yet stator Fucia running with a sapphire rotor has 35 times the stall torque density and 8 times the power density of the Namiki motor. Stator Green with a sapphire robot compares even more favorably to the Namiki in stall torque density. Its stall torque density is 48 times larger. Most importantly, however, is that the typical operating speeds of ultrasonic motors are much lower, granting a significantly better impedance match for nearly all loads.

Thick Film PZT: Penn State Materials Research Laboratory

Overview

The Penn State Materials Research Laboratory proposed to fabricate ferroelectric thick films on silicon substrates for subsequent piezoelectric ultrasonic micromotor development at MIT, and its integration into microrobotics. The idea is to develop an actuator technology that would enable integrated machines, a technology whereby an entire robot could be fabricated on a single piece of silicon in one batch fabrication process.

Actuator	Stall Torque (kgf-cm)	No-load Speed (rpm)	Power Density (W/kg)	Stall Torque Density (Nm/kg)	Peak Eff.
[Micro Mo] 1319E003	0.034	13,500	106	0.29	71%
[Mabuchi] FK-280-2865	0.16	14,500	NA	0.42	53%
[Namiki 92] 7CL-1701	0.0016	9,100	13	0.06	50%
Aeroflex	0.10	4,000	NA	0.04	20%
Maxon	0.13	5,200	NA	1.13	70%
Astro	0.76	11,500	NA	0.21	20%
[Kumada 85]	13.5	120	80	8.8	80%
[Shinsei 89] USR-80	6.0	125	23	3.4	35%
[Panasonic 87] USM-40	0.8	800	NA	1.1	40%
[Hosoe 89] EF35-135	1.2	80	NA	2.3	40%
MIT 8 mm Fucia	0.0055	1750	108	2.1	NA
MIT 8mm Green	0.01	870	NA	2.9	NA

Figure 14. This representative sampling of electromagnetic DC motors (without gears), commercially available Japanese ultrasonic motors and our 8 mm ultrasonic motors are presented to give a feel of relative measures of stall torque density and efficiency. Stators Fucia and Green are run with plain sapphire rotors.

This collaboration between MIT and Penn State University was an outgrowth of an earlier effort in which the viability of ferroelectric thin films, that were 0.3 μm thick, in ultrasonic micromotors has been demonstrated on micron-thick silicon nitride membranes [Flynn et al. 92], [Udayakumar et al. 94]. In this proposed effort, thick films have been fabricated by the screen printing technique which, through the use of patterned screens, would facilitate fabrication of stator structures of various geometries and thus minimize semiconductor processing.

The most limiting factor in applying screen printing technology to deposit thick lead zirconate titanate (PZT) films on silicon substrates was the film firing temperature. For micromotor applications, high temperature sintering is necessary to produce a dense PZT film that is capable of operating in the flexural mode. On the other hand, the commonly used silicon substrate is coated with a platinum metallization layer which serves both as a diffusion barrier layer and as a bottom electrode to the PZT film. Such platinum-coated silicon substrate have a maximum film processing temperature above which the blistering of the platinum layer becomes a problem. This temperature limit, for the most robust substrates, was about 850°C for a duration of few minutes, with a more desired and conservative value of 750°C at which the duration time could be more than an hour.

While conventional sintering usually takes place above 1000°C for PZT powder compacts, to overcome the temperature limitation imposed by the substrate materials, the proposed strategies were to use sintering aids such as (1) glass frit, (2) low melting eutectic compounds, and (3) fine particles, to reduce the film sintering temperature. The first two involve adding the PZT powders with additives that form a liquid phase at some elevated temperatures, but lower than the conventional sintering one, to facilitate the film densification process. Such liquid-phase sintering techniques are a commonly adapted method to achieve low temperature sintering. On the other hand, since the driving force for the sintering process is the reduction of the powder surface area, greater driving force can be achieved by using powders of smaller sizes. Therefore, powders produced from the hydrothermal method having submicron size have also been used in this effort of reducing the film sintering temperature.

Experimental Methods

Commercially available lead zirconate titanate powders from Morgan Matroc, and a submicron PZT powder with a Zr/Ti ratio of 53/47 were used as the functional piezoelectric materials. These powders had compositions close to the morphotropic phase boundary, and were known to exhibit peak dielectric and piezoelectric properties in the bulk. Amongst a number of glass frits and sintering additives that have been attempted, a 4 wt% of the 50 mol% Li_2CO_3 - 50 mol% Bi_2O_3 the glassy composition,

and a 9 wt% of the 83.5 mol% PbO - 16.5 mol% WO₃ eutectic system (m.p. 730°C) provided the best electrical characteristics, and only these are discussed here.

The PZT powder was mixed with the additives in a mill for 24 hours to reduce the average particle size of the powders, and then screened through a 200 mesh sieve. The dielectric paste was obtained by mixing the active powders with a proprietary DuPont organic vehicle, and modifying the viscosity and printability of the paste by dispersing with a-terpineol solvent. The homogeneity of the paste was enhanced by blending the mixture in a three-roll mill. The levels of the constituents in the paste were 69% by weight of the primary functional component (PZT), 22% organic vehicle, and 9% a-terpineol. The viscous dielectric paste was screen-printed through the apertures of a stencil screen to deposit the required pattern onto a 25-mm square platinum-metallized polycrystalline alumina substrate, or a (100) silicon wafer, with 500 nm thermally grown oxide, sputter coated with 150 nm platinum on a 20 nm titanium adhesion layer.

After the screen-printed films were allowed to level, they were dried at 110°C for an hour to remove the solvent by evaporation, and fired for 15 minutes at a peak temperature of 850°C. The organics are believed to burn-out in the neighborhood of 550°C during firing. The thickness of the film in a single pass was 12 µm. Multiple printings, dryings, and firings yielded thicker films. An Alpha-Step 100 profilometer from Tencor Instruments was used to record the film thickness profiles. A scanning electron microscope (SEM) was used to characterize the film microstructure.

Top contact electrodes of platinum, approximately 1200 Å thick, in varying sizes were sputter deposited to form a capacitor structure. Dielectric permittivity and loss tangents were measured on an Hewlett Packard 4274A multi-frequency LCR meter. The ferroelectric hysteresis behavior was examined with a modified Sawyer-Tower circuit, from which the remanent polarization and coercive field were determined.

Results

Initial emphasis was placed on the densification of the screen printed PZT films. A polycrystalline alumina substrate was used for higher temperature firing that cannot be tested with silicon substrate. The effects of various additives and starting powders were mostly examined by electron microscope for the microstructure, and by electrical properties measurements because better properties were expected for denser films.

Furthermore, since the use of additives to achieve low temperature sintering is usually at the expenses of the electrical properties of the PZT materials, it is ideal that the additives present in the final film should be as little as possible. Because of this concern, the searching for possible eutectic compositions has been based on the following two criteria to keep the impact from the additives on the materials properties at a minimum:

(1) the elements of the additives should be able to be incorporated as much as possible into the PZT perovskite ABO_3 lattice at the end of sintering, such as the $PbO-WO_3$ system where Pb could go into the A site and W into the B site; or (2) part of the elements constituting the sintering aids could escape from the PZT films at the end of sintering, such as the $PbO-PbF_2$ system with the evaporation of the fluoride at high temperatures.

Figure 15 shows the cross-sectional view of the microstructure of the screen printed PZT films using 4 wt% of equal molar $Li_2CO_3-Bi_2O_3$ glass frit. The fired film was about 12 μm in thickness. The film was deposited on a silicon substrate and fired at 850°C for 15 minutes. Although the various electrical properties have been characterized and the g_{33} coefficient was measured and comparable to the bulk materials [Chen 95], the film was obviously not fully densified. While this type of microstructure could be viewed as a PZT-air composite and might be suitable for some sensor applications, it was not ideal for the micromotor application in which a film capable of operating in the flexural

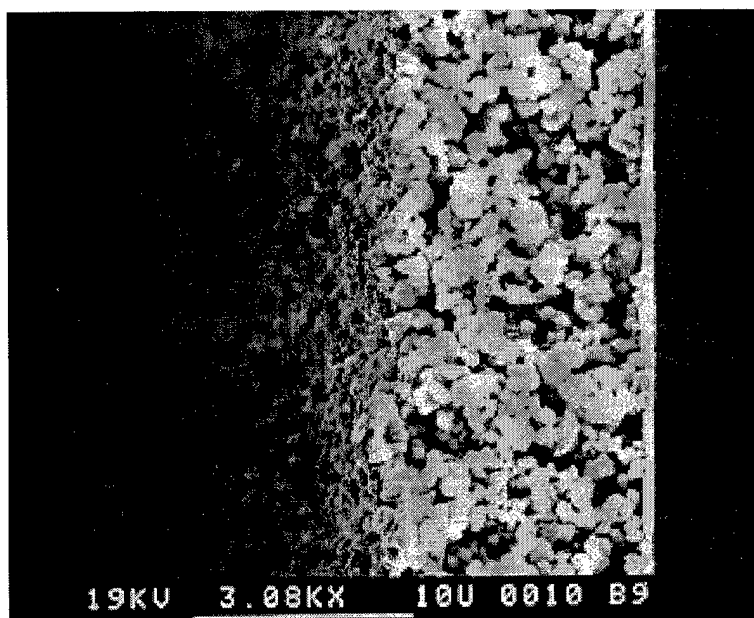


Figure 15. Scanning electron micrograph of the cross-section of the screen printed PZT films with 4 wt% equal molar $Li_2CO_3-Bi_2O_3$ glass frit addition. The film was deposited on a Pt-coated silicon substrate with a heat treatment at 850°C for 15 minutes.

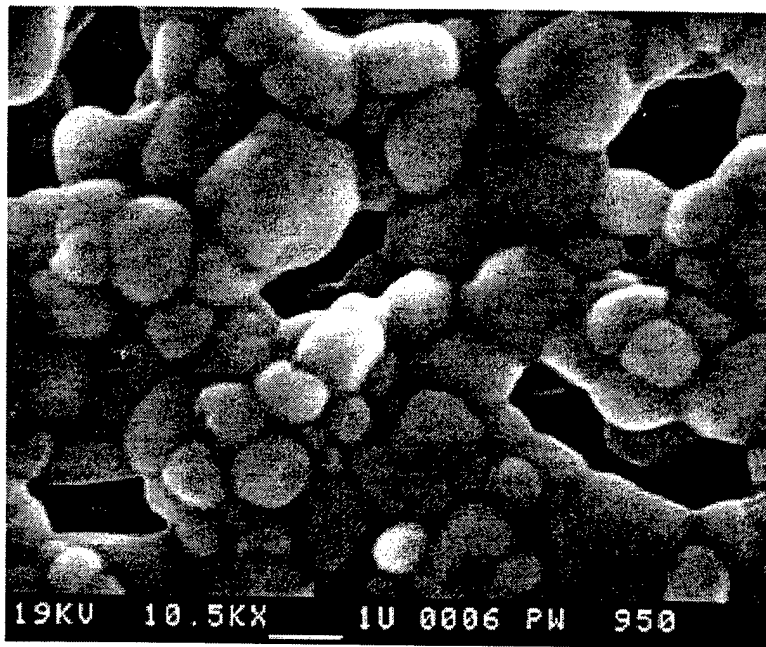
mode was necessary.

As to the use of a low melting point eutectic composition, the most extensive study and best results were obtained through the use of the $PbO-WO_3$ system as described

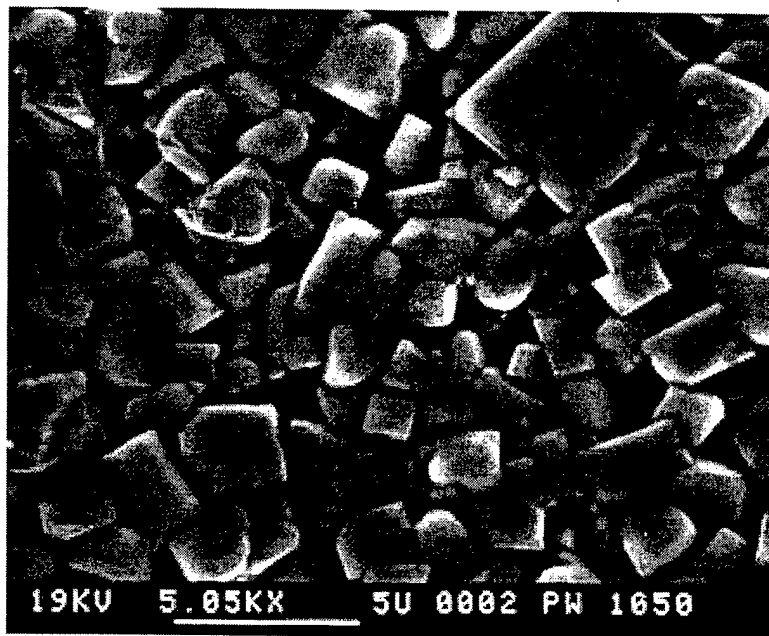
in the preceding section. Figure 16 shows the scanning electron microscopic images of the films heat treated at different temperatures and soaking times.

As can be seen in the 950°C/1hr sample, Figure 16(a), formation of the liquid phase in this film is rather obvious. Particles of the PZT powders are all uniformly wetted by the introduced liquid phase materials. The overall microstructure is porous and a three-dimensional skeleton with interconnected voids are demonstrated. Since sintering of this film is limited without much grain growth, the starting powders may be estimated from this picture to have a mean particle size of about 1 μm .

Figure 16(b) shows the same film fired at 1050°C for 1 hour. Under this sintering condition the film is fully densified, and the liquid phase has retreated below the surface of the film. Dramatic change in the shape of the grains, from the starting spheroidal to cubic, and the increase in grain size from initial 1 μm to about 2-3 μm size can be seen in Figure 15.



(a)



(b)

Figure 16. Microstructure of PbO-WO₃ liquid phase sintered PZT film surfaces. Heat treatment conditions are: (a) 950°C, and (b) 1050°C, both for 1 hour.

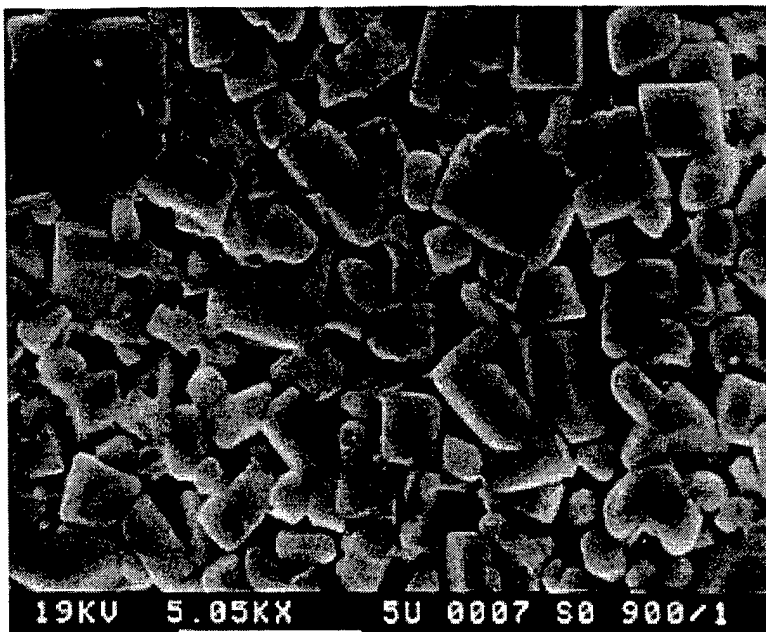


Figure 17. Microstructure of screen printed films using hydrothermal PZT powders and sintered at 1000°C for 1 hour. Substrate is Pt-metallized Al₂O₃.

Fine powders of 0.2 μm size produced from a hydrothermal process have also been used as the starting powders without the introduction of any additives, and was screen printed onto platinum metallized alumina substrates and heat treated at 1000°C for 1 hour. The densified microstructure of this film is shown in Figure 17. Compared to the results shown in Figure 16, the increased sinterability of the PZT powders could obviously be seen. All grains have a cubic shape similar to those shown in Figure 16(b), however, the average grain size is smaller due to the smaller starting powder.

Figure 18 shows the large signal P-E hysteresis loop of hydrothermal powder. With E_C of 17.9 kV/cm and P_R of 23.3 μC/cm². This is a significant improvement from the earlier commercial powders added with sintering aids. A word of note here is that the reproducibility of these film properties is rather poor and requires further verifications. Nevertheless, the enhanced sintering behavior by using fine PZT powders is of no doubt.

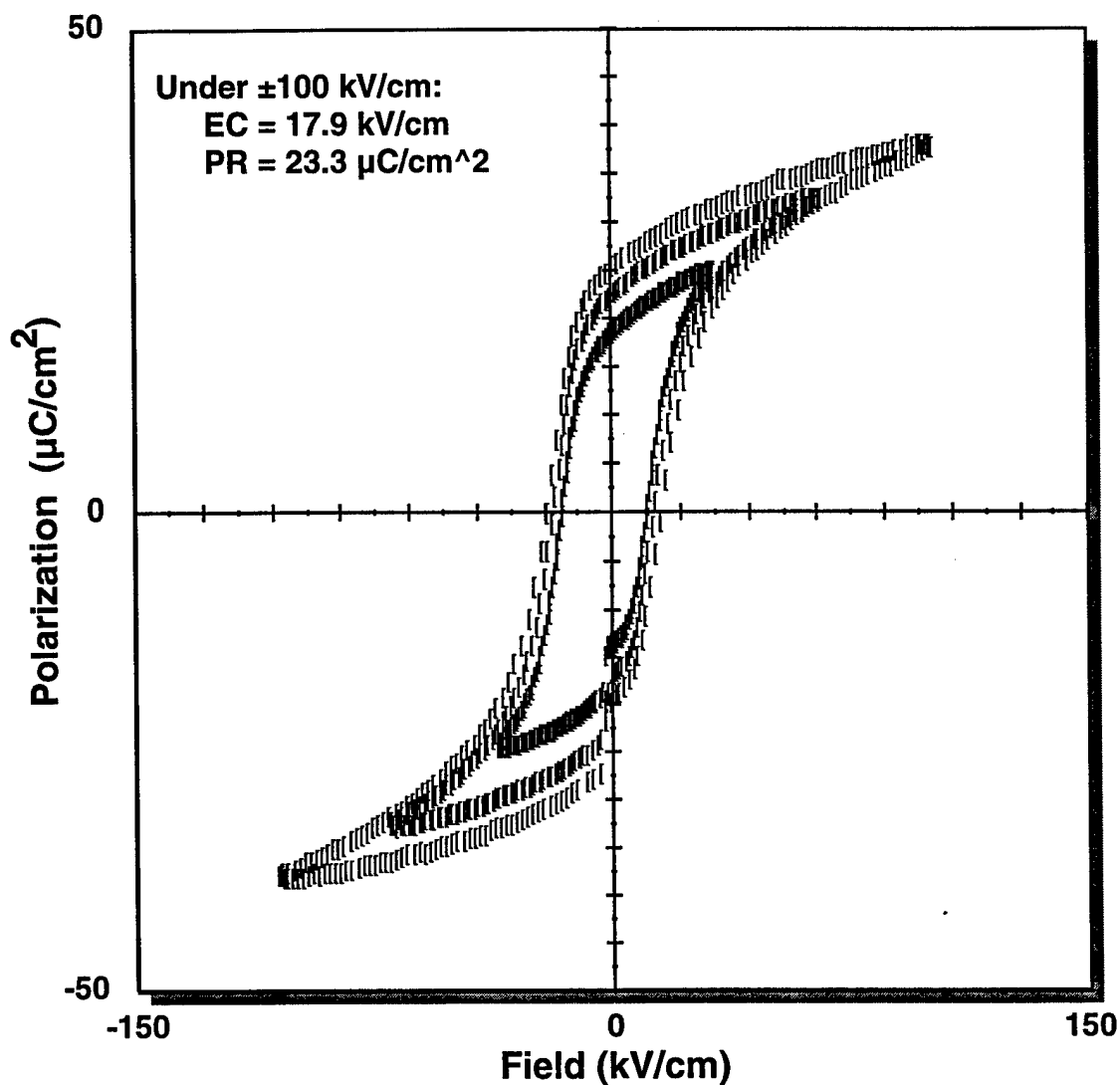


Figure 18. Large-field P-E hysteresis loop of screen printed PZT 53/47 film using hydrothermal powders, measured at 50 Hz.

The electrical properties of various films are summarized in Table 1. It is apparent that the higher the processing temperature the better the electrical properties, as denser films are expected. Generally speaking, screen printed PZT films with better properties have been constantly produced over the investigation period, however, to be able to utilize the screen printed films on the silicon substrates, more effort has to be made. At the current stage, the energy barrier in sintering these films to full density is too high to be processed on the silicon substrates.

Table 1. Summary of the Electrical Properties of Screen Printed PZT Films.

PbO-WO ₃ Content (wt%)	Temp./Time (°C) / (min.)	Dielectric Constant	Loss Factor	P _R /E _C /E _{max} (μC/cm ²) / (kV/cm) / (kV/cm)
0/Pt-Si	800/30	90	0.03	1.1 / 40 / 150
0/Pt-Si	850/15	120	0.04	1.1 / 40 / 150
11/Pt-Si	800/30	220	0.07	3.2 / 40 / 150
11/Pt-Si	850/15	200	0.05	2.6 / 44 / 150
20/Pt-Si	800/30	215	0.07	3.2 / 45 / 150
20/Pt-Si	850/15	280	0.06	4.0 / 50 / 150
11/Al ₂ O ₃	900/15	>300	0.03	9.5 / 25 / 100
11/Al ₂ O ₃	950/60	630	0.03	3.8 / 15 / 50
11/Al ₂ O ₃	1050/60	710	0.03	7.5 / 18 / 50
Plain Hydrothermal Powder	1000/60	900	0.03	23.3 / 18 / 150

Summary

The behavior of the liquid-phase-sintering can be affected by four factors: (1) melting point of the liquid phase, (2) amount of liquid phase, (3) time of sintering, and (4) characteristics of the starting materials (PZT and liquid phase). A couple of screen printed PZT films have been delivered for further evaluations of their properties for the proposed application.

From the above results on the eutectic PbO-WO₃ system, with a constant 1-hour heat treatment, the temperature at which significant densification was observed, i.e., 1050°C, was approximately 300°C higher than its eutectic point (730°C). This is because in order to achieve liquid-phase enhanced sintering, not only the eutectic compositions have to form the liquid phase in the first place, but also the surface tension of the liquid phase has to be low enough to wet the particles to be sintered. The wetting behavior provides an important capillary force at the particle joints through which sintering is promoted. Therefore, the temperature at which the liquid phase was effective would be considerably higher than just the eutectic point of the composition.

Conclusions

Autonomous Endoscopes and Ultrasonic Motors

For locomotion mechanisms for an autonomous endoscope, the radially oriented centrally driven belt-drive design has shown the most promise in its ability to crawl through intestine-like environments. This design lends itself quite nicely to miniaturization with the availability of smaller motors. The problem of how to avoid entanglement with the intestines still needs to be solved in order to have true feasibility of the device. A type of cow-pusher shield could be fitted to the frame in front of the area where the treads meet the sprockets in order to avoid entanglement. One of the larger problems left to solve is finding a suitable power source for the device that can be made small enough to correspond to the thumb-sized goal of the project. With the development of piezoelectric micromotors however, the efficiency and therefore the power requirements of the device will improve. The current design could be even further miniaturized with these motors as a result of the elimination of the central section for the reductions and motors. Ideally, each individual tread would have a motor driving its sprockets.

The 8 mm ultrasonic motors manufactured from bulk PZT show high prospects for such applications. If we compare these new ultrasonic motors to the smallest commercially available electromagnetic motors, the Namiki 7CL-1701 motors, which are 7 mm in diameter and 18 mm long, roughly 5 times the volume of the 8 mm ultrasonic motor, we find that the Namiki motor has a stall torque of 1.6 mNm, giving a stall torque density of 0.06 Nm/kg. Our highest-torque 8 mm motors display 10 gf-cm of stall torque, or 1.0 mNm, in a 0.34 g package, yielding a stall torque density of 2.9 Nm/kg, *a factor of 50 improvement over the Namiki motor.*

While these numbers appear encouraging for the possibilities of miniaturizing autonomous endoscopes, a number of challenges remain. The motors developed to date do not contain bearings and mounts, but rather were characterized in a dynamometer which supplied the bearing. Bearings, coupling mechanisms and appropriate packaging must be designed to make useful component motors. Additionally, the bulk ceramic form of PZT requires a two-phase 60 V_{peak} excitation which is supplied through high-voltage op-amps. Better power electronics and drive circuitry must be designed for compact motors to be used in autonomous microrobots.

Thick Film PZT

Advantages of using hydrothermal, submicron size, PZT powders are obvious from this study. It is quite natural that the next step from this point would be introducing sintering aids into this powder. Since the liquid-forming compositions used were obtained from commercial sources which normally have particle sizes larger than that of PZT powder itself, distribution and packing of these liquid-phase compositions within the small PZT powders will be of great concern. Besides reducing the liquid-forming

compositions' particle sizes by traditional milling and grinding, using these materials in their liquid organic precursor forms compatible with the printing paste formulation may be a suitable and desired alternative.

It would also be worthwhile to pursue other techniques that are able to increase the reactivities of the PZT powders or the liquid phase additives. Smaller PZT particle size, and a more uniform dispersion of the liquid phase within the starting films are among the possible routes to enhance the sinterability of the printed PZT films, and are hence deserved considerations for future studies.

References

[Chen et al. 95] H.D. Chen, K.R. Udayakumar, L.E. Cross, J.J. Bernstein, and L.C. Niles, "Dielectric, ferroelectric, and piezoelectric properties of lead zirconate titanate thick films on silicon substrates," *J. Appl. Phys.*, 77 [7] 3349.

[Fieguth et al. 94] "Conformal Design of Experiments: An Automated Tool Supporting Experiment Design and Analysis for Efficient Improvement of Products and Processes," Paul W. Fieguth, Michelle S. Spina and David H. Staelin, *MIT Leaders for Manufacturing Program Technical Report*, March 10.

[Flynn et al. 92] "Piezoelectric Micromotors for Microrobots," Anita M. Flynn, Lee S. Tavrow, Stephen F. Bart, Rodney A. Brooks, Daniel J. Ehrlich, K.R. Udayakumar and L. Eric Cross, *IEEE Journal of Microelectromechanical Systems*, Vol. 1, No. 1, pp. 44-51, March.

[Flynn 95] "Piezoelectric Ultrasonic Micromotors," Anita M. Flynn, Ph.D. Thesis in Electrical Engineering and Computer Science, Massachusetts Institute of Technology, May, 1995.

[Franck 95] "Manufacturing Ultrasonic Minimotors," Dean Franck, Bachelor's Thesis in Mechanical Engineering, Massachusetts Institute of Technology, May, 1995.

[Hollerback et al. 91] "A Comparative Analysis of Actuator Technologies for Robotics," John M. Hollerbach, Ian W. Hunter and John Ballantyne, *In Robotics Review 2*, MIT Press, Edited by Khatib, Craig and Lozano-Perez.

[McLurkin 95] "The Ants: A Community of Microrobots," James D. McLurkin, Bachelor's Thesis in Electrical Engineering, Massachusetts Institute of Technology, May, 1995.

[Shectman 95] "Autonomous Endoscope Propulsion," Arthur N. Shectman, Bachelor's Thesis in Mechanical Engineering, Massachusetts Institute of Technology, May, 1995.

[Udayakumar et al. 94] "Ferroelectric Thin Film For Piezoelectric Micromotors," K.R. Udayakumar, S.F. Bart, A.M. Flynn, J. Chen, L.S. Tavrow, L.E. Cross, R.A. Brooks and D.J. Ehrlich, *Ferroelectrics*, Vol. 160, pp. 347-56.

Appendix A: Autonomous Endoscope Propulsion

The following appendix contains excerpts from a bachelor's thesis written by one of the contributors to this project, Arthur N. Sheckman [Sheckman 95], and outlines in detail the variety of mechanisms that were investigated for traversing a large intestine.

Chapter 1

Introduction

Endoscopy today is a fairly invasive procedure in which the gastroenterologist must push an endoscope up through a person's large intestine. A current endoscope is about $\frac{1}{2}$ inch in diameter and resembles an extension cord in cross section and stiffness. The doctor must accomplish this insertion by brute force and the help of the end three inches of the device which are articulated with two degrees of freedom. This leads to a great deal of twisting and pushing in order to force the scope to follow the convolutions of the intestinal tract. On the other end the patient experiences a great deal of pain when it becomes necessary to distend the intestines in order to force the scope around its many bends and switchbacks. In some cases the intestine contains a complete loop, and in such cases the procedure can not proceed. The small intestines are also a region that for many gastroenterologists is unreachable. Their much tighter convolutions combined with their smaller diameter make them nearly impossible to explore using current endoscopic tools. The best gastroenterologists can only penetrate about 15cm into the small intestine. On average the doctor makes a trip of 4.5 meters into the large intestine in 15 to 25 minutes.

The desire to improve the device came from three main influences. The first being the wish to decrease the amount of pain and discomfort that the patient experiences during the procedure. The second came from ARPA(Advanced Research Projects Agency) which is currently funding the project. The Autonomous Endoscope Project is a part of a larger project that is trying to develop a remotely operated mobile

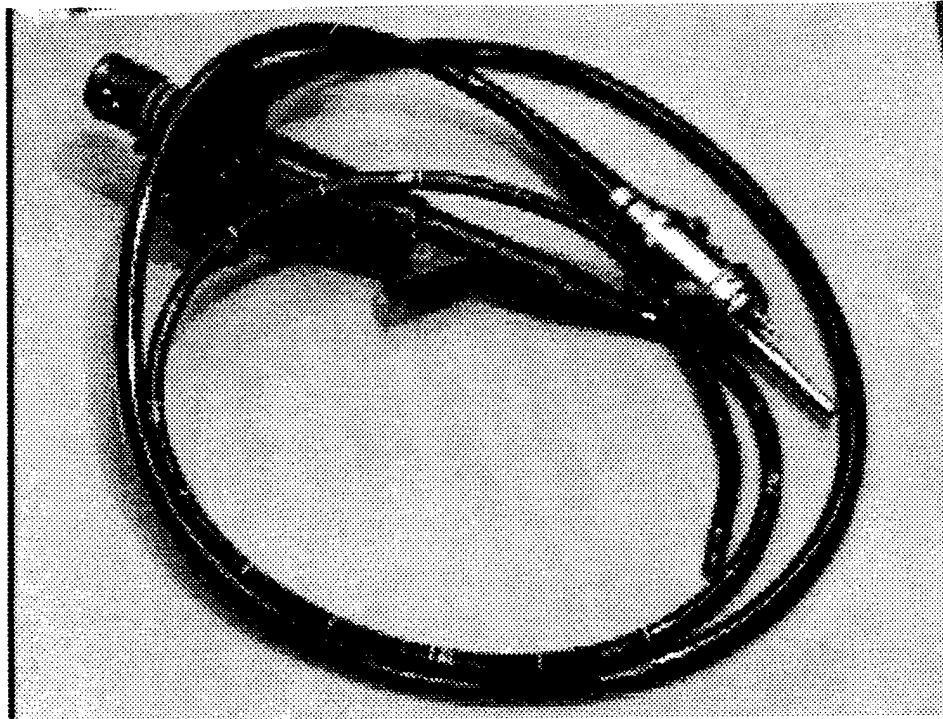


Figure 1-1: An Endoscope.

surgical vehicle. The vehicle would have all the devices of a modern surgery room, yet they would be modified in order to allow their tele-operation by a surgeon or doctor from a remote location. The third influence also stems from the ARPA project. In the future after endoscopic technology is proven, it is hoped that with the invention of smaller more efficient motors and actuators, a further round of miniaturization can be performed and the endoscopic vehicle can be inserted into the small intestines and possibly larger vascular tissues. Miniature integrated robotic systems, and actuators are being developed in parallel with the endoscope.

1.1 Design Constraints

In order to push forward in the design process a very rigid yet not necessarily specific design objective was required. The objective that was specified for the project was to create an autonomous endoscopic device with the approximate dimensions of 2cm in diameter, and 10cm long. In other terms this meant that the device had to be self contained and tele-operable as well as being no bigger than your thumb. With

this rigid goal defined it was possible to identify some of the primary constraints surrounding the problem. The first and foremost requirement for an autonomous endoscope is a system for propulsion. In the development of the project to date this has been the main focus of the design iterations. Care has been taken to insure that design revisions have been thought through with respect to the other constraints. This will facilitate later addition of systems in order to satisfy the other requirements of endoscopy.

1.1.1 Physical Properties of the Intestinal Environment

It was necessary to develop a system which could function in the adverse conditions inside the intestine. The intestine is evacuated prior to any endoscopic procedures, and is in a collapsed state. The inside of the intestines are covered with mucus and as a result are very slippery. An experimental determination with a cow intestine of the coefficient of kinetic friction μ_K led to a value of approximately 0.1. The intestines are also extremely flexible. In the evacuated state the intestines are a gathered tube without an open center having an undistended diameter of 3cm. In their maximum state of distension they can reach 13cm before rupturing. In the cecum, the largest part of the large intestine, the intestine is regularly 8-12cm without any distension. In addition to this flexibility of diameter, the intestines are only supported with respect to the body in a few locations. This leaves the intestine free to translate, rotate and coil within the body cavity.

1.1.2 Propulsion Requirements

There are three main design constraints associated with the propulsion system of an autonomous endoscope. The first being the need for a power source. The autonomous nature of the scope requires that the power source be small enough to fit inside the intestines and be light enough for the scope to drag it along with it. The source must also contain enough energy for the device to travel 4.5 meters into the intestines, perform diagnostic and surgical functions on the patient, maintain visual and telemetry

communication with the outside of the patients body, and have enough power left to travel out.

The second requirement is that the system be able to cope with the unsupported nature of the intestinal environment. The propulsion of the device needs to be achieved without causing the distension to any great degree of the intestines, yet be able to cope with areas that have varying undistended diameters. The worst case scenario that we used as an aid in design decisions was that the device should be able to make its way up a vertical tube of undistended intestine and be able to stop and perform diagnostic and surgical operations at any point.

The third constraint involved the physical structure of the intestines. The intestinal surface had to remain undamaged as a result of the propulsion mechanism. This meant that only limited pinching and point loading of the intestine was acceptable, and that any entanglement with the driving elements had to be avoided.

1.1.3 Vision System Constraints

The field of vision necessary for most endoscopic evaluations is a hemisphere located in front of the scope. The system must be able to cleanse itself in order to maintain the clarity of images in a mucus laden environment. A means of sending the information outside of the body is also necessary. One novel option might be a laser transmission system which is currently under development at Lincoln Labs. A test was performed using this system where video images were sucessfully sent through a 4cm thick steak. The system must also be able to operate within the power levels available from the scope's power source.

1.1.4 Tooling Requirements

There is an array of endoscopic tools that are currently used in procedures from biopsies to polyp removal. A universal tool, or a modular array of tools must also be produced in order to perform all of these operations. These tools must be able to perform their functions throughout the same hemisphere that the vision system

encompasses. The tools also must operate within the power boundaries set by the power source of the scope.

Currently endoscopes have a supply of gas that is vented through their tip in order to inflate the intestines in the area that is being examined. We have proposed that a bubble of air could be inserted with the device and the bubble could either move along with the device as it travels up the intestines, or it could be a large enough quantity of gas such that the entire large intestine became minimally inflated.

1.2 Elements of Propulsion

In order to fully understand the standpoint from which design decisions needed to be made a fundamental look at the nature of intestinal propulsion was taken. To begin with propulsion was qualified. It can be seen as the acceleration of a mass in a system. In the case of the intestines this acceleration is against the frictional and resistive extensional forces produced by the device moving through the intestine. This acceleration in a qualitative sense needs to be caused by a force. This force is the resultant of the frictional force on the scope and its own propulsive force. Here it is necessary to look at the nature of both of these forces in an intestinal environment. Both of these forces are based upon a frictional coefficient and a normal force. Contrary to intuition, the normal force provided by the intestine does not increase significantly with distension up until the painful limits of distension are reached. The elastic nature of the intestine provides a pressure which creates a normal force. In terms of the frictional force, the entire radial surface area is subject to this pressure. With respect to the driving force, only the area of the driving elements is used in the calculation of the propulsive force. The maximum propulsive force is limited by the frictional force in between the driving elements and the intestine; at its limit, slippage occurs. Therefore propulsive force is maximized with maximum propulsive area. This can be seen better by viewing the intestines as providing a pressure on the scope, and through the relation of pressure to force by area:

$$Force = Pressure * Area \quad (1.1)$$

we can see that the only way to increase the propulsional force based on the constant intestinal pressure is to increase the area of the propulsive elements. Another benefit received from the increase in the propulsive area is that it also leads to a decrease in the frictionally resistive area of the scope, thereby decreasing its minimum required propulsive force even further.

Chapter 2

Testing Environments

In order to evaluate the prototypes that were constructed it was necessary to develop means of simulating intestine like conditions. Several different tests were created in order to select for progressively more realistic conditions. Each prototype was evaluated in all of the testing environments. They proved an invaluable aid in qualifying the design flaws of each prototype and created a focus for the next round of prototyping. A description of each of the three environments that were created follows.

2.1 Half Pipe

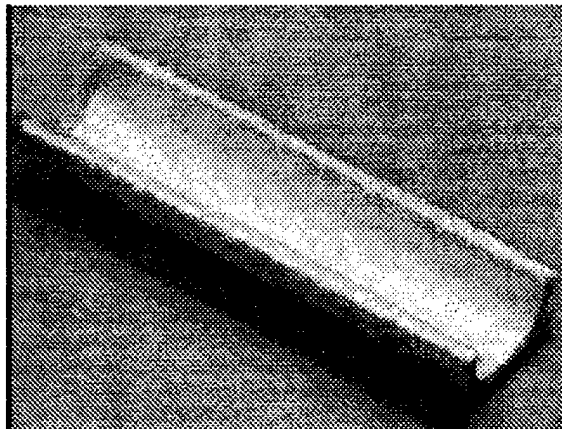


Figure 2-1: Half Pipe Testing Environment.

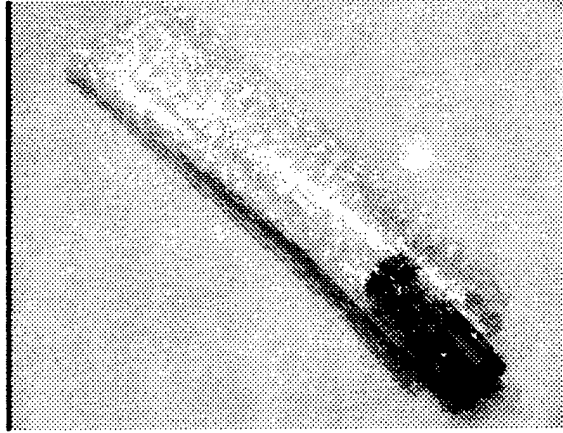


Figure 2-2: Tube Testing Environment.

The Half Pipe was designed to simulate the generally cylindrical nature of the surface on which the scope would have to propel itself. It consists of a layer of bubble wrap hot glued down to a lengthwise half section of cardboard tubing. The half cylindrical shape was chosen in order to allow viewing of the operation of the scope to as high of a degree as possible while still providing a semi-cylindrical environment for propulsion. The half pipe served as a test bed for gaining power and efficiency data as well.

2.2 Tube

The Tube environment was simply a bubble wrap tube of a slightly larger diameter than those of the prototypes. The diameter had to be slightly larger as a result of the relative inelasticity of bubble wrap. This environment was used to evaluate each prototype's performance in a fully surrounded environment, as well as enabling ease of testing the device through all of its radial orientations with respect to a gravitational normal. The tube was also utilized to evaluate the turning ability of the prototypes. In these tests the tube could simply be bent to effect a turn in the scope's path, or a section could be pinched in to shorten the distance that parts of the device would have to travel on one side of the turn. This was useful in evaluating the effects produced by the differential distances around the inside and outside of a turn in the intestines and how the scope would be able to cope with these differences.

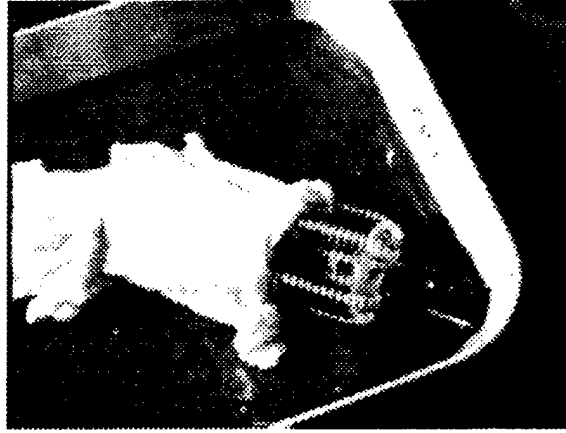


Figure 2-3: The Chicken Skin and Jell-O simulated Intestinal Environment.

2.3 Simulated Intestine

A Simulated Intestine was also constructed. This environment aimed at simulating the intestines to the highest degree possible. True intestines are extraordinarily odiferous and in consideration for the others in the lab we devised this substitute.

To begin with several chicken legs were skinned and the skins were collected. Next a pan full of soft red jell-o was made of approximate dimensions: $\frac{1}{2}$ inch deep by 10 inches wide by 14 inches long. The chicken skins were then stapled together to form a 7cm diameter 35 cm long intestine like tube. The fat deposits and irregularity of the skin formed a fairly close approximation to actual intestinal surfaces and the residual fat worked well as a substitute for the mucus that normally coats the intestines. For testing the tube was place on the tray of jell-o in order to simulate the unsupported nature of the intestines in the body cavity.

Testing in this environment illustrated each device's ability to open gathered intestines and travel through them in an unsupported environment. This was also the hardest test in terms of entanglement. The random fatty deposits and the flimsy and irregular nature of this tube in comparison to the bubble wrap made it much easier for the skin to become entangled in the propulsion elements.

Chapter 3

Prototype Description

Over the course of the year span of the project six prototypes have been constructed. Each of the first three prototypes was limitedly evaluated in order to establish the extent of their functionality. The main stress in conception of the ideas integral to each prototype was simply propulsion. The issues of miniaturization and tooling have been left for after an acceptable method of propulsion has been divined from our iterative design process.

As a result of this focus, all of the prototypes have been constructed from predominantly stock parts that are readily available. The mean size of the prototypes was constrained small enough to preserve the order of magnitude of size that the final scope must be however it was also maximized to the approximate size of a cow intestine. The use of cow intestine was seen as the final test for any of the prototypes because it is so readily and inexpensively available and provides a close approximation to the environment to be found in a human intestine.

An additional concern that justified the large scale prove-out of the prototypes was the high cost of miniaturization. It did not seem economically viable to develop small scale gears and frames at very high cost in order to construct a non-functional prototype. These expenses are best saved for the final result of the design process.

3.1 Preliminary Radial Drive Prototypes

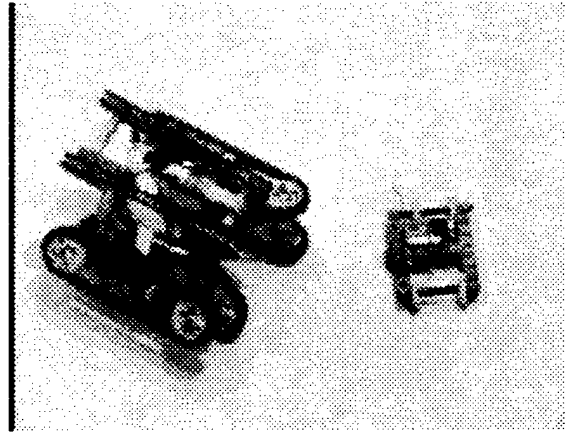


Figure 3-1: Early Prototypes: Number 1 on left. Encasable Drive on right.

The first prototype constructed was a vehicle with three separate Mabuchi servomotors geared down in order to drive a pair of treads each. They were assembled radially around a cylindrical aluminum frame, and the treads ran through the center of the cylinder and then out and around its length. This idea was inspired by a mockup created by Dean Franck (MIT '95) in which several rings were mounted in a cardboard frame on rotary pivots. Upon seeing and handling this mockup Colonel Richard Satava, a surgeon and gastroenterologist with the Army, who was representing the Advanced Research Projects Agency, expressed approval of this concept. The biggest problem at this stage was how to actuate these rings. This led to the development of the aforementioned prototype. This device will be referred to as Number 1.

Number 1 performed well and served to bring many problems to light in the process of building a system of drives around a hollow cylinder. Issues of alignment and end gear width are extremely important, as well as the tread width with respect to the curvature of the frame. It was found that an optimal number of six driven treads provides the best arrangement. This first prototype was able to crawl through a mock-up intestinal tube created out of rubber, and was able to move itself through a folded bend in the tube by advancing along the tube and straightening it out as the robot fed forward and turned. In this way no folds were left closed, and this could provide a full view of the intestines.

An attempt was made to encase a propulsion mechanism in a latex bellows.

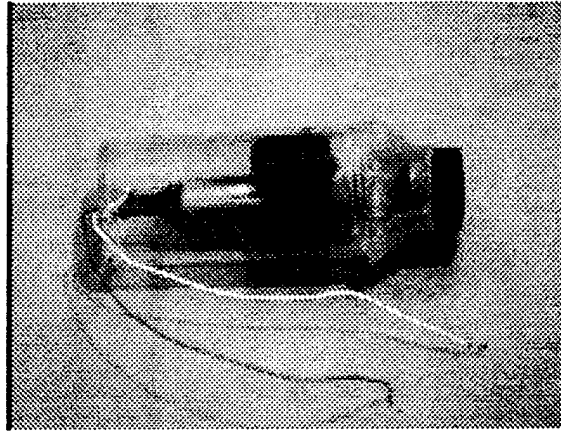


Figure 3-2: Impacting Mass Drive Prototype (Thumper).

A bellphragm can be envisioned by imagining a sock turned inside out on itself with the propulsion mechanism being located between the two layers. The second prototype's main purpose was to evaluate the feasibility of enclosing the entire robot in latex in order to increase the drive surface.

By increasing the area of the drive surface the robot would also maximize its frictional force with the intestinal wall and thus its maximum drive force. Unfortunately the problem of gathering the latex after it has been driven off of and recycling it through the center of the robot is a difficult task. In the testing of the second prototype, the latex continually became wedged between perpendicular sets of drive chains and stopped the prototype from moving. In some extreme cases the chains were pulled off the drive gears.

3.2 Thumper

The failure of the encasement of the radial drive prototypes left the question of how to create propulsion of the device without relying solely on friction to do so. After reading a Paper on an Impacting Mass Drive by Toshiro Higuchi, this method of propulsion looked like it would function well in the intestine. An Impacting Mass Drive consists of a friction plate, and an actuator capable of accelerating a mass, and the mass itself. The device takes advantage of the differences between the static

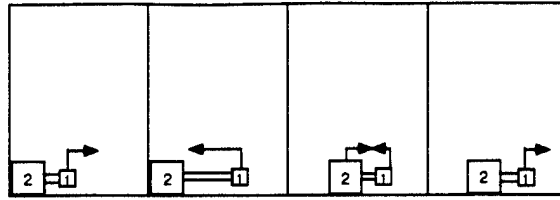


Figure 3-3: Stages of the Impacting Mass Drive Cycle.

frictional force and the kinetic frictional force created by its frictional plate. By accelerating the mass slowly creating a force just below the static frictional force holding the plate in place, kinetic energy can be stored in the accelerating mass. At the end of the actuator's stroke the acceleration of the mass is impulsively reversed to the highest degree attainable from the actuator. This high acceleration in the opposite direction produces a force great enough to break the plate free of the static frictional force holding it in place. Once the plate is sliding, the frictional force is much lower, and the device slides to a halt. After this the actuator slowly repositions itself in order to repeat the cycle.

The prototype that was constructed used a plastic vile as the frictional plate with and piezoelectric stack actuator mounted concentrically to the inside of the cylinder. Attached to the other end of the acutator was a steel mass to serve as the driving mass of the system. A small lense was also fitted to the vile.

3.2.1 Basic Iterative Simulation

In order to predict the best ratio of the mass of the plate to the mass of the driving weight, and to predict displacement values per cycle for the Thumper a simple iterative simulation was developed in matlab. The theory behind the simulation is presented here.

Definition of Variables and Constants

To begin with a list of the variables to be used in the theory is needed.

$$g = 9.8 \left(\frac{m}{s^2} \right)$$

$\mu_s = 0.3 =$ Coefficient of Static Friction between Thumper and Intestines

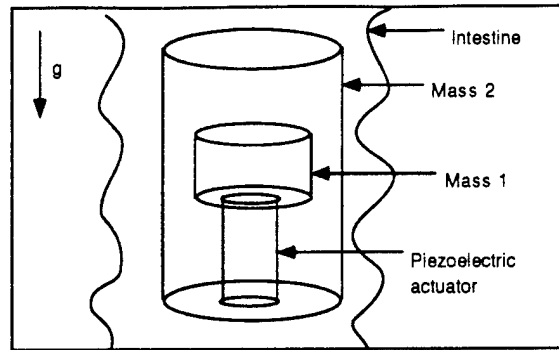


Figure 3-4: Simulation Setup.

$\mu_k = 0.1 =$ Coefficient of Kinetic Friction between Thumper and Intestines

$V_1 =$ Velocity of mass 1 with respect to mass 2 ($\frac{m}{s}$)

$V_{1,max} =$ Maximum Velocity of mass 1 with respect to mass 2 ($\frac{m}{s}$)

$a_1 =$ Acceleration of mass 1 with respect to mass 2 ($\frac{m}{s^2}$)

$x_2 =$ Displacement of mass 2 with respect to inertial (m)

$V_2 =$ Velocity of mass 2 with respect to inertial ($\frac{m}{s}$)

$a_2 =$ Acceleration of mass 2 with respect to inertial ($\frac{m}{s^2}$)

$F_a =$ Accelerating Force on mass 1 defined positive as mass 1 moves against gravity (N)

$F_R =$ Resultant Force on mass 2 from accelerating mass 1 (N)

$N =$ Normal Force (a function of pressure and area) (N)

$F_{\mu_s} =$ Frictional Force between the Thumper and the Intestines (N)

$F_{max\mu_s} =$ Maximum Static Friction Force ($\mu_s \times N$) between the Thumper and the intestines (N)

$stroke_d =$ The maximum displacement of the piezoelectric stack due to an applied voltage.(m)

$stroke_t =$ The time it takes the Piezoelectric actuator to move $stroke_d$ (s)

Theoretical Analysis of Impacting Mass Drive

In order to begin the simulation, first we must determine the maximum static frictional force on the Thumper. In order to maximize the movement of the Thumper

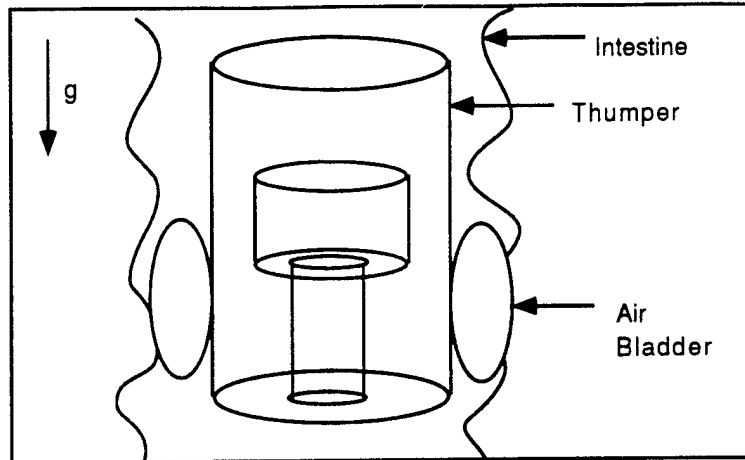


Figure 3-5: Air Bladder Operation.

we must maximize the energy put into the system. In order to do this we must first determine the maximum allowable acceleration that can be given to mass 1 without the resultant force moving the Thumper backward.

We assume that gravity has no effect upon the normal force regardless of the orientation of the device as a result of the unsupported nature of the intestines. We also assume that the pressure between the Thumper and the intestines can be kept at a constant 0.1 psi through the use of an air bladder.

By inflating or deflating the bladder it will regulate the amount of distension that the intestines undergo and through this the air bladder can regulate the pressure on the Thumper.

The first step is to convert the pressure in psi to N/m^2 using a conversion factor of $6.895 \times 10^3 \frac{N}{m^2 psi}$, we get a pressure of $689.5 \frac{N}{m^2}$. We also know that:

$$Force = Pressure \times Area \quad (3.1)$$

So we need to calculate the surface area of the Thumper. We have modeled the Thumper as a cylinder of radius: $R = 0.01$ m and height: $L = 0.1$ m. The surface

area of a cylinder is governed by the equation:

$$\text{Surface Area} = 2 \times \pi \times R \times L \quad (3.2)$$

$$\text{Surface Area} = 2 \times \pi \times (0.01) \times 0.1 = 6.28 \times 10^{-3}(\text{m}^2) \quad (3.3)$$

So now calculating the normal force we get:

$$\text{Normal Force} = 6.283 \times 10^{-3}(\text{m}^2) \times 689.5\left(\frac{\text{N}}{\text{m}^2}\right) = 4.332(\text{N}) \quad (3.4)$$

and to convert this to $F_{\text{max}\mu_s}$, we multiply the normal force by the coefficient of static friction μ_s ,

$$F_{\text{max}\mu_s} = \mu_s N = 4.332 \times 0.3 = 1.3(\text{N}) \quad (3.5)$$

Now that we have the $F_{\text{max}\mu_s}$, we can calculate the maximum allowable acceleration for the internal mass (mass 1). Remembering:

$$\text{Force} = \text{mass} \times \text{acceleration} \quad (3.6)$$

We can see that the resultant force on mass 2, F_R generated by accelerating mass 1 should not exceed the maximum frictional force on mass 2, $F_{\text{max}\mu_s}$, in order to prevent the Thumper from slipping backwards. That is during the extension phase of the piezo stack, mass 2 is held stationary as long as the resultant force on mass 2, F_R , is less than $F_{\text{max}\mu_s}$. $F_{\text{max}\mu_s}$ is dependent solely on the normal force applied by the intestines and the coefficient of static friction. Dynamically the force on mass 1 is governed by $F_a = m_1 a_1$ where $F_a = -F_R$. The condition for mass 2 to remain stationary during extension of the piezo stack can be expressed by this force balance equation:

$$m_1 \times a_{1\text{max}} = F_{\text{max}\mu_s} - m_2 \times g - m_1 \times g \quad (3.7)$$

which sets the maximum force allowable on mass 1 equal to the sum of the gravitational forces acting on both masses and the frictional force acting on the Thumper,

where $a_{1_{max}}$ is the maximum allowable acceleration before the Thumper slips backwards.

We then get for an acceleration boundary equation:

$$a_{1_{max}} = \frac{F_{max\mu_s} - m_2 \times g - m_1 \times g}{m_1} \quad (3.8)$$

Once $a_{1_{max}}$ is determined, if we extend the piezo stack at a constant acceleration of this value, we can determine the velocity of mass 1 at the end of the extension stroke. Noting that $Velocity = Acceleration \times Time$ when the initial Velocity and Displacement are zero, we can see that in order to determine the maximum velocity of mass 1, $V_{1_{max}}$, we need to find the time it takes the piezoelectric stack to go through its displacement in one stroke. The interval is called the stroke time $stroke_t$. The stroke distance $stroke_d$ is a constant based on the piezoelectric stack. For our simulation, $stroke_d = 1.8 \times 10^{-5}$.

To calculate $stroke_t$, remember:

$$distance = \frac{1}{2} \times acceleration \times time^2 \quad (3.9)$$

$$stroke_d = \frac{1}{2} \times a_{1_{max}} \times stroke_t^2 \quad (3.10)$$

solving for $stroke_t$ we get:

$$stroke_t = \sqrt{\frac{2 \times stroke_d}{a_{1_{max}}}} \quad (3.11)$$

Now recall for our Maximum Mass 1 Velocity Equation:

$$Velocity = Acceleration \times Time \quad (3.12)$$

Therefore:

$$V_{1_{max}} = a_{1_{max}} \times stroke_t \quad (3.13)$$

Once we know the velocity of mass 1 at the end of the stroke, $V_{1_{max}}$, we can use the

principle of conservation of momentum to calculate the velocity of mass 2. Here we assume that the velocity of mass 2 with respect to inertial can be modeled as a perfect collision between mass 1 moving at $V_{1_{max}}$ and mass 2 at rest. From the law for the conservation of momentum:

$$m_1 \times V_{1_{max}} = (m_1 + m_2) \times V_{2_{max}} \quad (3.14)$$

or

$$V_{2_{max}} = \frac{m_1 \times V_{1_{max}}}{m_1 + m_2} \quad (3.15)$$

This however is the maximum instantaneous velocity of the Thumper body directly after the transfer of energy from m_1 to $m_1 + m_2$. In reality, V_2 will be higher than the $V_{2_{max}}$ calculated this way. In our formulation we have actually taken a conservative estimate. The reason being that in this model, for conservatism it is assumed that after the energy transfer m_1 and m_2 are traveling in the same direction with the same velocity. In actuality, the driving function of the piezoelectric stack will reverse the acceleration on m_1 with respect to m_2 , effectively trying to reverse the direction of m_1 by pulling harder forward on m_2 . This will slow down m_1 with respect to the inertial speed of m_2 , thereby transferring more energy to m_2 and subsequently increasing V_2 beyond the $V_{2_{max}}$. (This is a conservative estimation of the true dynamics).

Next we assume the transfer of energy from m_1 to m_2 through the piezoelectric actuator can be modeled by assuming the stack behaves as a stiff linear spring. First we must determine the spring constant "K" for the piezo/spring model. Noting that Young's modulus for the actuator stack = $4.4 \times 10^{10} \left(\frac{N}{m^2}\right)$, we can calculate K. K has units of Force per length $\frac{N}{m}$ so :

$$K = \frac{\text{Young's Modulus} \left(\frac{kg \cdot m}{s^2 \cdot m^2}\right)}{\frac{\text{Length}}{\text{Area}} \left(\frac{m}{m^2}\right)} \quad (3.16)$$

Where "Area" is the cross sectional area of the stack and "length" is it's length. Knowing this, we can determine the deformation of the spring model by an energy balance where we assume the energy is transferred from m_1 into the piezoelectric

stack instantaneously without a resulting movement of m_2 .

So:

$$\frac{1}{2}m_1V_{1_{max}}^2 = \frac{1}{2}Kx_{piezo}^2 \quad (3.17)$$

where x_{piezo} is the expansion of the stack due to the impact of mass 1 at the end of the stroke, and not as a result of any voltage applied. This gives us:

$$x_{piezo} = \sqrt{\frac{m_1}{K}}V_{1_{max}} \quad (3.18)$$

Now we need to determine the acceleration of m_2 to asses wheter or not the Thumper breaks free of Static Friction. Recall:

$$Velocity = Acceleration \times Time \quad (3.19)$$

and:

$$Distance = \frac{1}{2}Acceleration \times Time^2 \quad (3.20)$$

So:

$$Acceleration = \frac{Velocity^2}{2 \times Distance} \quad (3.21)$$

and so assuming a constant acceleration (a_2) throughout the collision:

$$a_2 = \frac{V_{2_{max}}}{2 \times x_{piezo}} \quad (3.22)$$

Now that we have calculated the acceleration of m_2 we convert that into a Force forward on the Thumper.

$$-F_{R_{max}} = (m_1 + m_2) \times a_2(\text{constant throughout collision}) \quad (3.23)$$

m_1 is added to m_2 here to account for the return push as m_1 is negatively accelerated. This is a big assumption but it its approximately the same magnitude as the conservative direction assumption previously about the return stroke of m_1 . Now that we have $F_{R_{max}}$ we need to compare it with $F_{max\mu_s}$.

If $F_{R_{max}} < F_{max\mu_s}$:

$$x_2(\text{displacement of Thumper}) = 0 \quad (3.24)$$

If $F_{R_{max}} > F_{max\mu_s}$:

then through a force balance:

$$(m_1 + m_2) \times \text{post collision } a_2 = N(\text{Normal Force}) \times \mu_K + (m_1 + m_2) \times g \quad (3.25)$$

that is quantitatively:

$$\text{Net forward force on } m_1 + m_2 = \text{Force of kinetic friction} + \text{Gravitational force} \quad (3.26)$$

where *post collision* a_2 is the constant deceleration that the frictional force and the force of gravity produce on $m_1 + m_2$.

Now that we have determined whether or not the Thumper actually breaks free of static friction we can now write the equation for its displacement when it does.

Recalling:

$$\text{Velocity} = \text{Acceleration} \times \text{Time} \quad (3.27)$$

we get:

$$\text{Time in motion} = \frac{V_{2_{max}}}{\text{post collision } a_2} \quad (3.28)$$

and plugging into:

$$\text{Distance} = \text{Velocity} \times \text{Time} + \frac{1}{2} \times \text{Acceleration} \times \text{Time}^2 \quad (3.29)$$

we get the final Thumper Displacement Equation:

$$x_2(\text{Thumper Displacement}) = V_{2_{max}} \times \text{Time in Motion} + \frac{1}{2} \times \text{post collision } a_2 \times \text{Time in Motion}^2 \quad (3.30)$$

Here we present a graph of the ratio of the two masses with respect to the displacement that will be achieved.

From the simulation we saw that it was the surface area of mass 2 that was

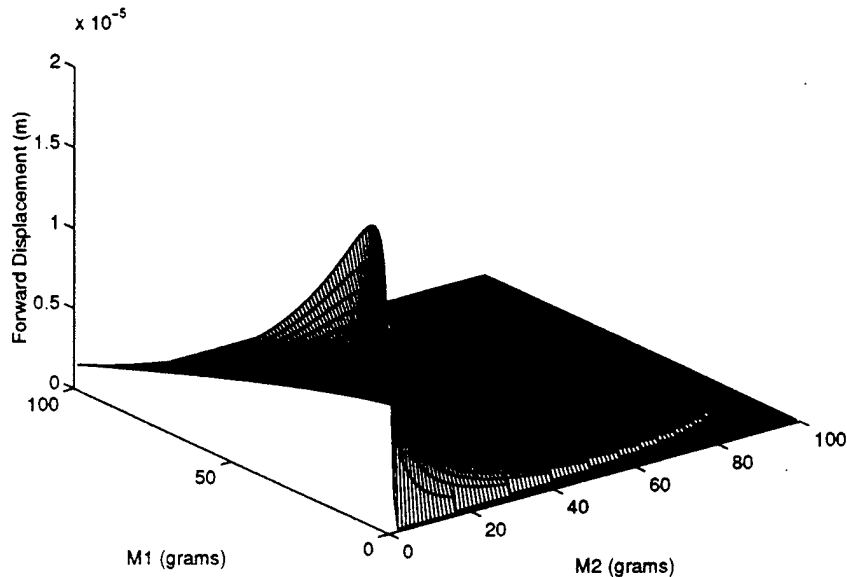


Figure 3-6: Optimization of Mass 1 and Mass 2 for Maximum Displacement of Mass 1 per Stroke.

important and the weight of mass 1. An optimum weight of about 37 grams was found for mass 1 with a corresponding mass 2 of 5 grams. This ratio of weight produced a forward displacement of 0.001mm per stroke.

3.3 Ethel

The next prototype constructed returned to more conventional propulsion methods. It consisted of a more centralized drive system and went back to a radial arrangement of driving elements. This prototype was named Ethel. Ethel's main design benefit was that only one motor was used to drive seven rows of driving elements. These elements were paddle wheels that meshed with a central drive worm. Through this mechanism 21 individual paddles could be driven off the one central worm. The motor and gear reduction were located inside this central worm in order to shorten the overall length of the scope.

This prototype utilized a 14mm diameter Micro Mo motor attached to a 256:1 reduction to power the drive worm. The worm itself effected a reduction of 4:1. The

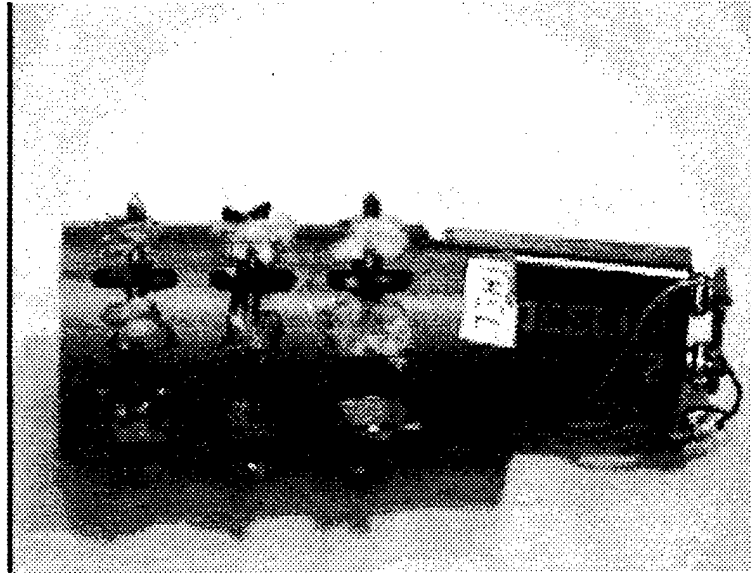


Figure 3-7: Scope Prototype Ethel.

motor was centrally located inside of a Delrin cylindrical case. The drive worm was also machined from Delrin to fit concentrically around this frame. In this way the overall length was shortened while providing a bearing surface for the drive worm to ride on. The base of the inner frame was then glued into an outer paddle wheel cage that served in mounting and positioning the individual paddles. A nine volt battery served as the powercell for the prototype, and was simply mounted to the end of the device.

Ethel operated with a total reduction of 1024:1, from a combination of the motor gearhead and the central worm drive. Ethel weighed in with a battery at 203 grams. The final dimensions for this prototype once the battery was recessed into the frame were; 50mm on the major diameter and 41mm on the minor diameter, with an overall length of 130mm.

3.4 Hercules

After the relative success in the preliminary evaluation of the worm drive with the significant decrease in prototype size that it allowed, it was decided to try to create a prototype with six centrally powered treads rather than paddles. The prototype

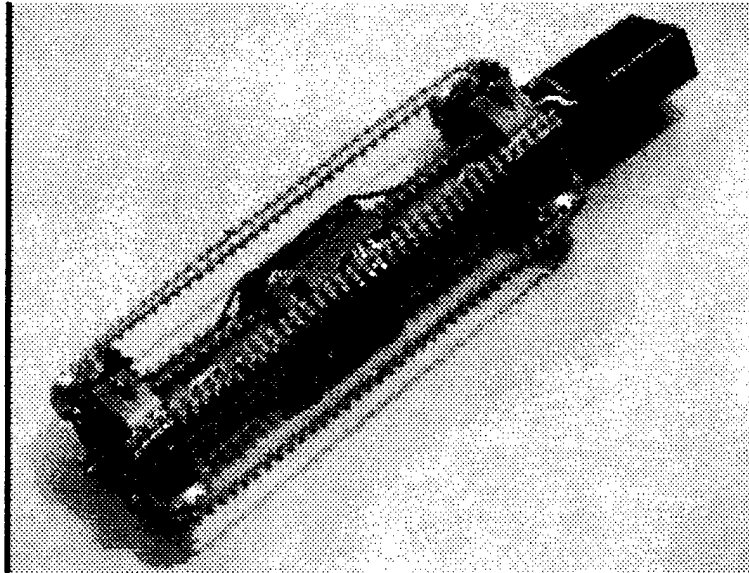


Figure 3-8: Scope Prototype Hercules.

named Hercules (seen above) did just that. Hercules used stock worms and worm gears in order to power six radially oriented treads of Berg "E-Z Chain". The scope was powered by 2, 10mm diameter Micro Mo 6 Volt motors that we ran at 9 Volts. These motors were centrally mounted within the Delrin/Teflon frame that was machined. The motors were located at either end of the frame with their output shafts oriented inward. Between the two motors, each with a 256:1 gearhead attached, was a double length worm. Six radially oriented worm gears were mounted in the frame around this worm, giving an additional 60:1 reduction. The gears were specially machined to have sprockets in their hubs in order to drive the treads. This provided another 2:1 reduction. The Delrin/Teflon mix was chosen for the frame material because of its bearing like low friction properties.

Hercules was driven at 9 Volts with a total reduction of 30,720:1. The total weight with battery of this prototype was 155.26 grams. Final dimensions on Hercules were a major diameter of 56mm and a minor diameter of 42mm, with a total length of 152mm.

3.5 Romulus

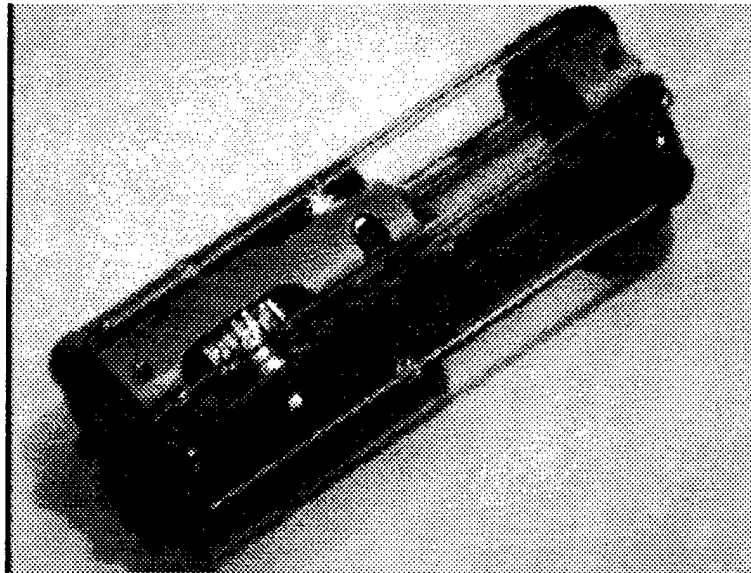


Figure 3-9: Scope Prototype Romulus.

With the success of the radially driven treads, it was decided to make an attempt with the stock parts on hand to miniaturize the scope. This was mainly in an attempt to identify the major issues of concern in miniaturization of the mechanism. To this end the prototype Romulus was created. It has the same mechanism as Hercules for propulsion with the exception of using elastomer polyethelyene belts rather than treads for driving off of. Some other differences are the addition of ball bearings in the end pulleys for the belts in place of the Delrin Bushings in Hercules' sprockets. The device also only utilized one motor with a 256:1 gearhead driving the same double length worm and worm gear setup. The exception here is that where the other worm gears had sprockets machined in their hubs Romulus has capstains that the belts were wrapped around in pretension.

The Belts came from a company called Pyramid, and were pretensioned with the suggested 17 percent extension. Romulus was driven with one Micro Mo 10mm 6 Volt motor driven at 9 Volts, with a total reduction of 15,360:1. Romulus has a major diameter of 34mm and a minor diameter of 31mm, with a total length of 90mm. Total weight with a battery for Romulus was 150 grams.

Chapter 4

Results

The last three prototypes constructed named Ethel, Hercules, and Romulus, were tested in order to try to quantify their relative strengths and weaknesses. Efficiency and Torque data we gathered on each prototype and velocity and aspect ratio data was also collected. A judgement on the tendency of each propulsion system to become entangled in the simulated intestinal environment was also made. A presentation of these results follows.

4.1 Efficiency and Power Evaluation

Each scope was placed in the half pipe with a series of loads in tow through a pulley arrangement. In this way the resistive force on the scope could be calculated. With a corresponding velocity measurement the utilizable power output of the propulsion system could be calculated. Current and Voltage data was also gathered at each load point. This data was used to calculate power input for each prototype at each load point. The ratio of Power in the utilizable Power out is also presented in efficiency versus load graphs for each prototype.

Looking into this data it was found that the average power input for the three prototypes were 0.685 Watts for Romulus, 1.52 Watts for Ethel, and 1.004 Watts for Hercules. Power out and efficiency data were not reasonably calculable from the tests performed. The data was gathered in the halfpipe environment where the scopes

Table 4.1: Load, Voltage, Current, and Speed Data

Ethel			
Load	Voltage	Current	Time
NL	8.0V	0.22A	3sec
11.3g	7.92V	0.21A	4sec
20.06g	7.88V	0.19A	4sec
25.5g	7.52V	0.19A	4sec
39.53g	7.4V	0.18A	7sec
42.5g	8.0V	0.18A	stall

Hercules			
Load	Voltage	Current	Time
NL	8.11V	0.13A	19sec
11.3g	8.03V	0.13A	19sec
20.06g	7.96V	0.13A	19sec
25.5g	7.96V	0.13A	19sec
39.53g	7.92V	0.13A	19sec
59.59g	7.82V	0.125A	23sec
70.89g	7.77V	0.11A	stall

Romulus			
Load	Voltage	Current	Time
NL	8.4V	0.07A	14sec
11.3g	8.6V	0.09A	22sec
20.06g	8.6V	0.09A	stall

Table 4.2: Average Power Input

Prototype	Ethel	Hercules	Romulus
Power In	1.52W	1.004W	0.685W

Table 4.3: Aspect Ratio Data.

Prototype	Ethel	Hercules	Romulus
Aspect Ratio	0.226	0.337	0.090

don't have maximum frictional coupling and more importantly geometric compliance to the surface. In the actual intestine the flesh drapes around the scope giving it a much better medium for coupling power out. In addition to this the unsupported nature of the intestine makes loading the scope and taking power out measurements almost impossible.

4.2 Aspect Ratio

In evaluating all of the prototypes it was determined that the aspect ratio of each was perhaps the most crucial design characteristic. The aspect ratio of the device is in a basic sense the difference between the major and minor diameters of each prototype. The larger the ratio the better the driving ability and the less frictional resistance each prototype was seen to exhibit. In a more particular light the aspect ratio is better calculated for comparison as follows. First a line must be constructed between two adjacent treads maximum radial dimensions. Then a line parallel to this must be constructed tangent to the minor diameter of the prototype. The radial distances to both lines are then subtracted. This is then normalized by dividing by the major diameter of the device. A table of values for this aspect ratio for the last three prototypes follows.

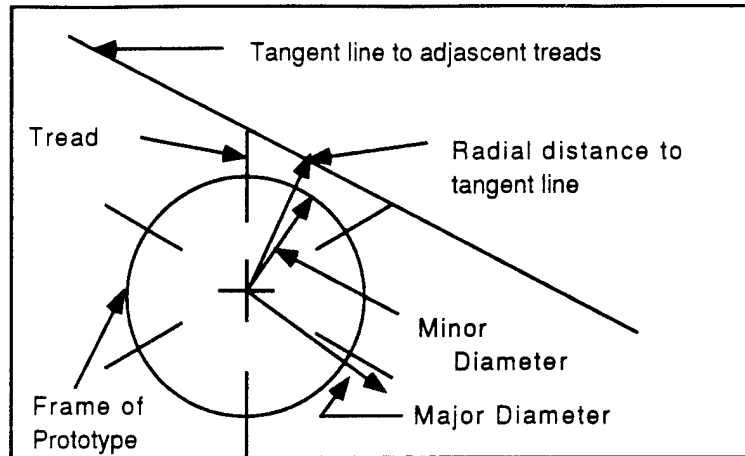


Figure 4-1: Aspect Ratio Determination.

4.3 Entanglement

In running each prototype through the simulated intestinal environment each one exhibited a different degree to which it became entangled in the chicken skin tube. Ethel was perhaps the most vivid in terms of entanglement. When the paddles would circulate inside the cage, skin would become trapped between the paddle and the cage and get pinched in. The pointed nature of the end of each paddle had devastating effects upon the integrity of the skin and the drive became so jammed with ripped skin that it stalled. Ethel has been given a very high entanglement rating. Hercules however faired much better. Entry into the tube and motion along the inside was easily accomplished on most of the trials. On one trial however at the point where the tread wraps around at the rear end of the device some skin became pinched between the tread and the sprocket and pulled back into the frame causing Hercules to stall. In consideration of this Hercules was given a mild entanglement rating. Romulus faired the best of the three with no real entanglements, however this is most likely a result of the very low coefficient of friction between the belts and the intestines. This resulted in their relative inability to drive Romulus through the simulated intestine, and gave very little opportunity to grip any portion of the skin hard enough to entangle it. Romulus was given a rating of no entanglement from these observations.

Table 4.4: Entanglement Data.

Prototype	Ethel	Hercules	Romulus
Entanglement	Very High	Mild	None

Chapter 5

Recommendations

The radially oriented centrally driven prototype design has shown the most promise in its ability to crawl through intestine like environments. This design lends itself quite easily to miniaturization with the availability of smaller motors and gearheads, and smaller gearing. The problem of how to avoid entanglement still needs to be solved in order to have true feasibility of the device. A type of cow-pusher shield could be fitted to the frame in front of the area where the treads meet the sprockets in order to avoid entanglement. Another possible solution would be to recess the end sprockets just over halfway into the frame thereby eliminating any meshing angles between the frame, tread, and sprockets that could lead to entanglement. One of the larger problems that is left to solve is finding a suitable power source for the device that can be made small enough to correspond to the thumb size goal of the project. With the development of piezoelectric micromotors however the efficiency and therefore the power requirements of the device will improve. The current design could be even further miniaturized with these motors as a result of the elimination of the central section for the reductions and motors. Ideally each individual tread would have a motor driving its sprockets. With these motors the size and performance goals of the project could no doubt be satisfied.

Bibliography

Publications:

H.D. Chen, K.R. Udayakumar, L.E. Cross, J.J. Bernstein, and L.C. Niles, "Dielectric, Ferroelectric, and Piezoelectric Properties of Lead Zirconate Titanate Thick Films on Silicon Substrates," J.Appl. Phys., v.77 n.7 p.3349 (1995).

H.D. Chen, K.R. Udayakumar, L.E. Cross, J.J. Bernstein, and L.C. Niles, "Development and Electrical Characterization of Lead Zirconate Titanate Thick Films on Silicon Substrates," ISIF '94, p.495 (1994).

Anita M. Flynn, "Piezoelectric Ultrasonic Micromotors," Ph.D. Thesis in Electrical Engineering and Computer Science, Massachusetts Institute of Technology, May, 1995.

Dean L. Franck, "Manufacturing Ultrasonic Minimotors," Bachelor's Thesis in Mechanical Engineering, Massachusetts Institute of Technology, May, 1995.

James D. McLurkin, "The Ants: A Community of Microrobots," Bachelor's Thesis in Electrical Engineering, Massachusetts Institute of Technology, May, 1995.

Arthur N. Sheckman, "Autonomous Endoscope Propulsion," Bachelor's Thesis in Mechanical Engineering, Massachusetts Institute of Technology, May, 1995.

Talks:

International Conference on Automation and Robotics and AI Applied to Analytical Chemistry and Laboratory Medicine, "Microrobots for Endoscopy," Anita M. Flynn, San Diego, CA, Jan. 16, 1996.

Berkeley Sensor and Actuator Center, "Ultrasonic Motors and Autonomous Endoscopes," Anita M. Flynn, University of California, Berkeley, CA, Nov. 28, 1995.

Personnel:

Anita M. Flynn, Graduate Student, MIT.

Dean L. Franck, Undergraduate Student, MIT.

Arthur N. Sheckman, Undergraduate Student, MIT.

James D. McLurkin, Undergraduate Student, MIT.

Prof. Rodney A. Brooks, Professor of Electrical Engineering and Computer Science, MIT.

Dr. Kewen K. Li, Postdoctoral Scholar, Penn State University.

Prof. L. Eric Cross, Evan Pugh Professor, Penn State University.